EFFECTS OF RANDOM ATOMIC DISORDER ON ELECTRONIC AND MAGNETIC PROPERTIES OF GRAPHENE NANORIBBONS

A Thesis Submitted to
the Graduate School of Engineering and Sciences of
İzmir Institute of Technology
in Partial Fulfillment of the Requirements for the Degree of

MASTER OF SCIENCE

in Physics

by
Korhan Ertan ÇAKMAK

July 2018
İZMİR

We approve the thesis of **Korhan Ertan ÇAKMAK**

Examining Committee Members:

Assoc. Prof. Dr. Alev Devrim GÜÇLÜ
Department of Physics, İzmir Institute of Technology

Assoc. Prof. Dr. Özgür ÇAKIR
Department of Physics, İzmir Institute of Technology

Prof. Dr. Bekir Sıtkı KANDEMİR
Department of Physics, Ankara University

3 July 2018

Assoc. Prof. Dr. Alev Devrim GÜÇLÜ
Supervisor, Department of Physics
İzmir Institute of Technology

Prof. Dr. R. Tuğrul SENGER
Head of the Department of
Physics

Prof. Dr. Aysun SOFUOĞLU
Dean of the Graduate School of
Engineering and Sciences

ACKNOWLEDGMENTS

I would like to thank the thesis supervisor Assoc. Prof. Dr. Alev Devrim Güçlü for his guidance, support and trust throughout this thesis. Even when I was stuck with the simple computational codes he was there for not only me for all the members of our research group. His encouragements were motivating, and his sincerity made everything possible. His support became the reason of my willing to learn and study more in the pursuit of excellence during this Master's thesis study. I am very proud that I had the chance to work with him. I also express in last three years that I have been collaborating with Abdülmenaf ALTINTAŞ, Hakan Ulaş ÖZDEMİR, Anıl KOLAY. Working with my group was also a pleasure for me. Also I would like to thank to my roommates and new groupmates; Mustafa POLAT, Elif ŞAHİN,and tea-crew, Gökhan ÖZTARHAN. Eventually, I want to express my gratitude to the most important people in my life, to my parents Hülya CENGİZ and Ayhan ÇAKMAK and also my grandparents Şadan Gezin and Muhlis ÇAKMAK was my endless source of motivation. All of them together made this thesis inevitable.

This work was supported by The Scientific and Technological Research Council of Turkey(TUBITAK) under the 1001 Grant Project No.114F331. The numerical calculations reported in this work were partially performed at TUBITAK ULAKBIM, High Performance and Grid Computing Center (TRUBA resources)

ABSTRACT

EFFECTS OF RANDOM ATOMIC DISORDER ON ELECTRONIC AND MAGNETIC PROPERTIES OF GRAPHENE NANORIBBONS

In this thesis, We investigate the effects of randomly distributed atomic defects on the magnetic and electronic properties of graphene nanoribbons with zigzag edges using an extended mean-field Hubbard model. We show that electron-electron interaction effects not only make defect states robust as compared with the tight-binding results,but also make edge states fragile even at low defect concentration for clean edge sites. For a balanced defect distribution among the sublattices of the honeycomb lattice in the bulk region of the ribbon, the ground state antiferromagnetism of the edge states remains unaffected. By analyzing the excitation spectrum, we show that while the antiferromagnetic ground state is susceptible to single spin flip excitations from edge states to magnetic defect states at low defect concentrations, it's overall stability is enhanced with respect to the ferromagnetic phase. Then, we investigated Anderson localization induced metal to insulator transition by a localization length in nanometer scale up to 5% vacancy concentration by using time dependent results. We found that, Anderson localization is stronger at the vicinity of Fermi level energy states since those states are becoming full of impurity states and edge states, mixed.

ÖZET

GRAFEN NANOŞERİTLERDE RASTGELE ATOMİK DÜZENSİZLİĞİN ELEKTRONİK VE MANYETİK ÖZELLİKLERE ETKİLERİ

Bu tezde, atomik düzensizliklerin ortalama-alan Hubbard modeli kullanarak zigzag grafen nanoşeritlerin (ZGNŞ) elektronik ve manyetik özellikleri üzerinde ki etkilerini araştırdık. Elektron-elektron etkileşiminin etkisi sadece düzensizlik durumlarını sıkıbağ sonuç-larına kıyasla güçlü kılmakla kalmıyor, ayrıca düşük düzensizliklerde zigzag kenarlar temizken bile kenar durumlarını daha kırılgan yapıyor. Nanoşeritin yığın bölgesindeki balpeteği yapısının altyapıları arasında dengeli dağılmış olan düzensizlikler için kenar durumların minimum enerjili antiferromanyetizm durumu etkilenmemektedir. Uyarım spektrumunu analiz ederek, minimum enerjili antiferromanyetik durumu düşük düzensizliklerde kenar durumlarından manyetik düzensizlik durumlarına tek spin dönüşümüne duyarlıyken, ferromanyetik faza göre tümden kararlılığın artığını gösterdik. Daha sonra, zamana bağlı sonuçlarımızı kullanarak Anderson lokalizasyonundan kaynaklı metal-yalıtkan geçişini nanometre düzeylerinde lokalizasyon uzunluğu ve %5'e kadar boşluk konsantrasyonu kullanarak gözlemledik. Anderson lokalizasyonunun Fermi seviyesi etrafındaki durumlarda, düzensizlik durumlarıyla kenar durumlarının tamamen iç içe geçip birbirleriyle karıştığından dolayı, diğer band bölgelerine göre daha fazla olduğunu bulduk.

TABLE OF CONTENTS

LIST OF FIGURES

Figure **Page**

LIST OF ABBREVIATIONS

TB . . . . . Tight-Binding
CVD . . . . . Chemical Vapor Deposition
FET . . . . . Field Effect Transistor
GNRs . . . . . Graphene Nanoribbons
HOMO . . . . . Highest Occupied Molecular Orbital
LUMO . . . . . Lowest Unoccupied Molecular Orbital
ZGNRs . . . . . Zigzag Graphene Nanoribbons
AFM . . . . . Antiferromagnetic
FM . . . . . Ferromagnetic

CHAPTER 1

INTRODUCTION

Carbon is the extraordinary and quiet essential element for many forms which are known from the ancient times (graphite and diamond). Graphene is the first material that is two-dimensional which gives to this material a unique set of properties. Since 1859, many scientists were looking for graphene using complex experiments. However, the first crystal of graphene were discovered in 2004 by using so simple and effective method called "Scotch tape method" at Manchester scientists who are Professor Sir Andre Geim and Professor Sir Konstantin(Novoselov et al. (2004)) noticed small parts of graphene on the tape used to clean a graphite stone. After this simple and ground-breaking experiment, they were awarded with the Nobel Prize in Physics in 2010. Thanks to "Scotch tape method", this area of science grew really extremely quickly. And today, hundreds of laboratories and theoretical approaches all over the world deal with different aspects of graphene research. Fig.(1.1) shows how the amount of papers about graphene has exploded in the last 20 years.

1.1. What is Graphene?

Theoretically, the first of the extraordinary features, the electronic band structure of graphene, was first studied by Wallace in 1947 (Wallace (1947)), and he explained its semi-metal behaviour due to the lack of an energy gap between the valence and conduction bands by using tight-binding approach (TB) . Moreover, at the point of these two bands meet, there is no density of states, which is believed to be the charge neutrality point where the Fermi level in the graphene sits at the Dirac point (Novoselov et al. (2004),Geim and Novoselov (2007)). Another important feature for graphene is its Dirac spectrum for massless fermions (Novoselov et al. (2005)). Eventually, due to the existence of zero-energy states, and having charge carriers like Dirac fermions provide and anomalous quantum hall effect with half-integer quantization (Novoselov et al. (2005),Yuanbo Zhang and Kim (2005)), instead of integer one (Klitzing et al. (1980)). This is the most direct evidence for Dirac fermions in graphene.

In general, the combination of unique properties such as; graphene is the first 2D

material ever known to us, the thinnest object ever obtained, and the lightest one, and also the strongest material, harder than diamond, and about 300 times stronger than steel, graphene conducts electricity much better than copper, graphene is a transparent material, graphene is bendable and can take any form you want, makes it magnificent material. Moreover, this magnificent material gave birth to a new class of crystals (MoS_2, BN, $(CF)_n$, $NbSe_2$, MgB_2, etc.) that are also just one atom thin, and also these can be shuffled with each other to engineer new materials on demand to meet the special needs of different industries. All these factors move graphene rapidly from the laboratories to the marketplaces driven by the men in industries where such magnificent materials are required for example, aerospace, automotive, electronics, energy storage, coatings and paints, communications, sensor, solar, oil, etc.(Crew (2018)).

1.2. Pristine Graphene

All these properties in previous subsection are considered, investigated and proved step by step in years. Therefore, it is better to start with the most fundamental element of the graphene to examine the other recently observed features.

1.2.1. Carbon allotropes

If we look at the simplest honeycomb model (Benzene ring, see (1.2)); we could see why we should study the gradients of graphene (Carbon atoms) and its properties as a starting point.

Carbon is the sixth most efficient element of the periodic table and is the piece of all organic molecules and, therefore, essential for life on Earth. The fundamental lectures from undergraduate education say that if carbon could be taken into account in the atomic ground state, 1s and 2s orbitals would be filled fully with up and down spins and 2 electrons would be in the 2p orbitals. Moreover, if the carbon is in the excited state, we could have 4 equivalent quantum-mechanical states called as; $|2s\rangle$, $|2p_x\rangle$, $|2p_y\rangle$ and $|2p_z\rangle$. A quantum-mechanical superposition of the state $|2s\rangle$ with n $|2p_j\rangle$ states is called spin hybridisation, that is important in covalent carbon bonds.

Sp^2 hybridization is the combination of graphitic forms. In sp^2 hybridization, the linear combination of two 2p (such as; $|2p_x\rangle$ and $|2p_y\rangle$) and $|2s\rangle$ orbitals creates 3 possible sp^2 quantum-mechanical states are given by;

$$
\begin{aligned}
\left|sp_1^2\right\rangle &= \frac{1}{\sqrt{3}}\left|2s\right\rangle - \sqrt{\frac{2}{3}}\left|2p_y\right\rangle \\
\left|sp_2^2\right\rangle &= \frac{1}{\sqrt{3}}\left|2s\right\rangle + \sqrt{\frac{2}{3}}\left(\frac{\sqrt{3}}{2}\left|2p_x\right\rangle + \frac{1}{2}\left|2p_y\right\rangle\right) \\
\left|sp_3^2\right\rangle &= -\frac{1}{\sqrt{3}}\left|2s\right\rangle + \sqrt{\frac{2}{3}}\left(-\frac{\sqrt{3}}{2}\left|2p_x\right\rangle + \frac{1}{2}\left|2p_y\right\rangle\right)
\end{aligned}
\tag{1.1}
$$

These orbitals are in the xy-plane and have 120^o angles. The unhybridized $2p_z$ orbital is in the z-plane and perpendicular to this (xy) plane.

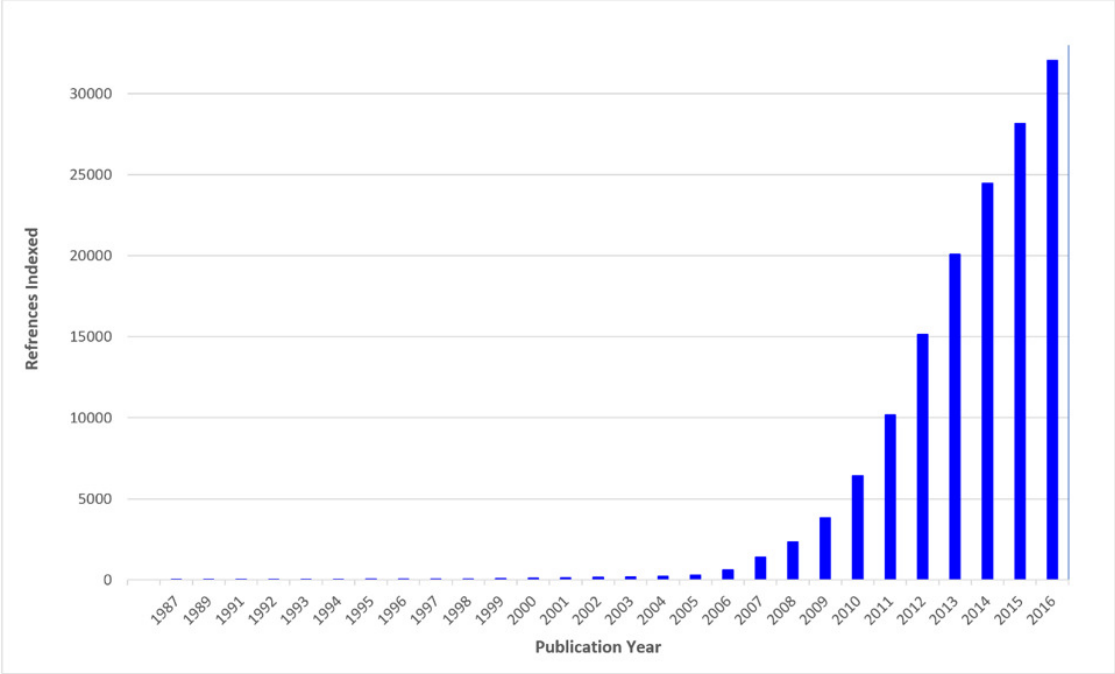

Figure 1.1. Number of academic publications referencing "graphene" in their text, per year between 1986 and 2016 as indexed by SciFinder (Source:Meany and Joseph (2017))

This is the molecular structure that has been proposed by a German chemist Friedrich August Kekulé in 1865 (Kekule (1865)). In this structure, six Carbon atoms join together by single bonds first form a chain. The chain closes to form a ring then comes six Hydrogen atoms and three double bonds and the benzene molecule is complete. The bonds between each Carbon atoms and Hydrogen atoms are σ bonds and also the remaining $2p_z$ orbitals form 3π bonds and resulting double bonds around the hexagon.

This balance of all bonds in benzene ring was explained by Linus Pauling in 1960 (Pauling (1960)).

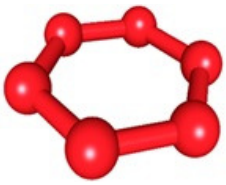

Figure 1.2. An honeycomb graphene lattice (Benzene ring).

The results after a plethora of research on these molecular structures showed that any graphitic allotrope include a graphene sheet at least own its construction. Historically, the oldest known allotrope is 3D graphite. Its discovery going back to the 16th Century and first property what was noticed, as anyone can guess, is for painting and writing usage. Although it is named later as "lead pencil" (like it is made of lead), in the middle of 18th Century graphite was discovered in the form of Carbon atoms and named as "graphite" just due to the fact that its main use for graphical purposes. However, graphite can be in the form of layered structure as a stacking of graphene sheets (see Fig.(1.4a)). These graphene layers have van der Waals bonds which is much weaker than the covalent bonds between the carbon atoms in each layer. This physical property explains the graphical purposes, "Scotch tape method" and exfoliation of graphene.

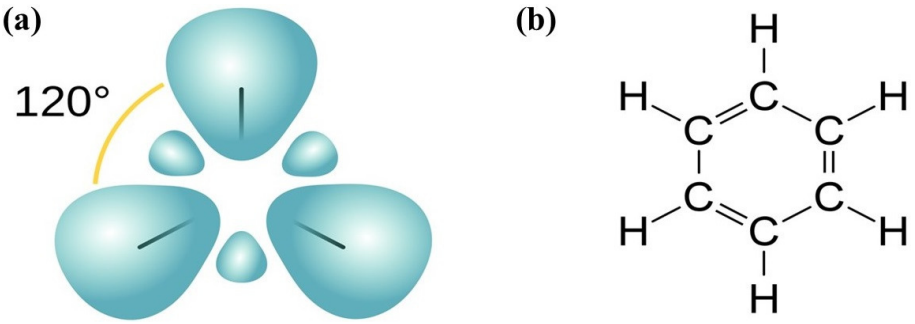

Figure 1.3. (a) Schematic side view of sp^2 hybridization. (b) Benzene Molecule (C_6H_6).

0D graphitic allotrope is C_{60} molecule which was discovered by Harold Kroto in 1985 (KROTO et al. (1985)). It looks like a football and named as "buckyball". It includes

graphene sheets, however some hexagons are replaced by pentagons which causes it has a formation of graphene sphere (Fig.(1.4(b))). As rolling up the graphene sheets give us 1D carbon nanotubes (Fig.1.4(c)), with a diameter of several nanometers.

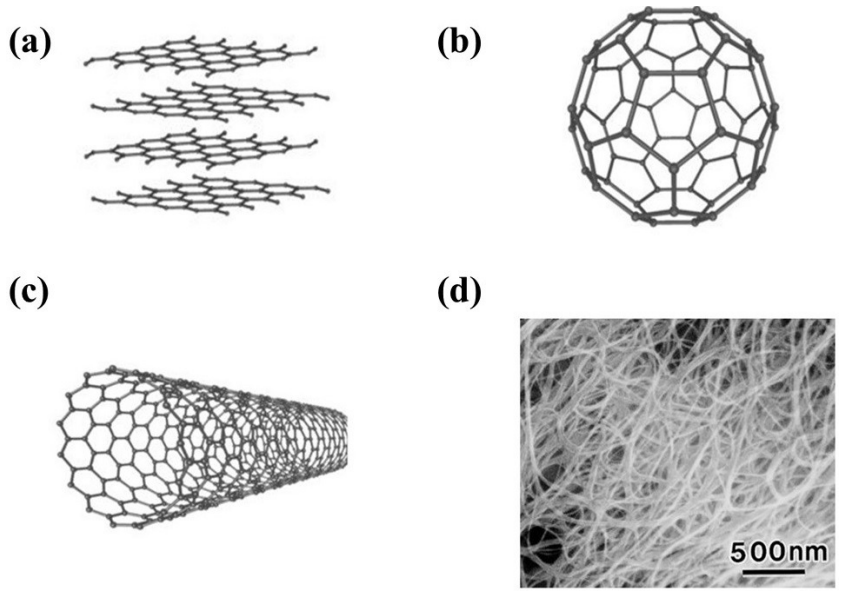

Figure 1.4. (a) Layered structure of graphite. (b) 0D allotrope: C_{60} molecule. (c) 1D allotrope: single-wall carbon nanotube. (d) SEM image of single-wall carbon nanotubes (source: NanoLab (2017)).

The discovery of carbon nanotubes is most often attributed to Sumio Iijima and his 1991 publication in Nature (Iijima (1991)). Started with the Iijima paper, there is a raising interest and plenty of researches all over the world about this compound in the condensed matter physics community and also in the prospect of nanotechnological applications, since today such a interesting functional material can be based in any science area from biomedical science for reparation of a part of a human body to the electronic device manufacture for a new monitoring systems for the environment.

1.3. Fabrication of Graphene

In this section below, the most popular ways in three techniques, chemical exfoliation, epitaxial growth and chemical vapor deposition (CVD) , used in fabricating graphene are discussed. In spite of high-quality graphene sheets have been offered by

these techniques, there are economical and quality differences between these methods.

1.3.1. Mechanical Exfoliation of graphene

As it is mentioned before, this is the first and basic method of obtaining graphene known as "Scocth Tape Method" , used by Geim and co-workers in 2004. Graphite includes parallel graphene sheets, which are bounded by weak van der Waals forces. Once a bit of graphite is scratched on a substrate, thin graphite stacks, which are mostly composed of tens or many graphene sheets, are peeled from the bulk and left behind on the substrate. Geim and associates accomplished expelling layers from a graphite flake by rehashed peeling (Novoselov et al. (2004)) until the color of tape becomes into shades of grey. The manufacture of graphene by this technique is, in this way, to a great degree straightforward. By peeling a little of graphite crystallite on the adhesive side of folded tape, the graphite piece is splited into two sections, which ends up more slender with a less number of graphene layers. After this process is repeated many times, the tape with the graphene sheets adhered to the Si/SiO_2 substrate, a blend composed of hydrochloric acid and hydrogen peroxide to obtain better the graphene sheets from the tape. At the point when the tape is precisely and gently peeled away, the graphene sheets stay stuck to the substrate. The darker locales, in which the wafers would be with thickness of around 300 nm, then as in Fig.(1.5) can be seen by using an optical microscope in the visible range, comprise of more graphene layers than the lighter ones. In any case, the sizes of these examples are in μm scale, which is should have been longer or larger-area for the use of graphene in labrotaroy applications and in commercial applications.

1.3.2. Epitaxial graphane

Walt de Heer and Claire Berger (Berger et al. (2004),de Heer et al. (2007)) created another strategy to manufacture graphene. They used thermal decomposition and surface science techniques. SiC (Silicon Carbide) has a similar hexagonal lattice symmetry with the graphene. By heating SiC wafers up to the temperature range of $1350^o - 1400^o$ C lead to dissipate the less firmly bond Si atoms from the surface, the rest of the carbon rebonds to frame monolayer or multilayers of graphene over SiC. By epitaxial process, it is possible to control the quantity of framed graphene layers. The subsequent electron mobility is maybe low, to such an extent that the surface is less decided for the creation of tests

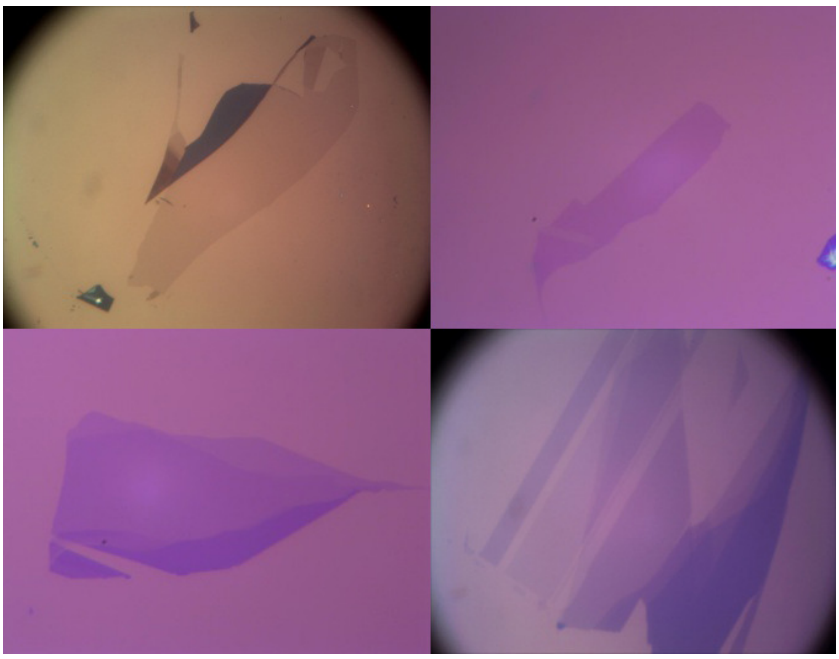

Figure 1.5. Microscope images of graphene flakes. Single and multiple layers of graphene showed by the darker regions, respectively. (source: Exfoliation (2018))

utilized in transport estimations. The graphitization procedure on C-ended is exceptionally quick, and countless layers are framed (up to 100). In addition, in this process, the electron mobility is high. In spite of the fact that this technique produces graphene in bigger scale with a high quality than exfoliation technique does, Since the high temperature, SiC is expensive substrate and lacking of exchanging graphene on another substrate are restricted this technique for applications (Choi et al. (2010)). Heating the SiC substrate causes Si atoms to be evaporated from the surface. Fig.(1.6(a)) shows that the graphisation process on the SiC substrate. These numerical distance values have been confirmed by X-ray measurements (Varchon et al. (2007)).

1.3.3. Chemical Vapor Deposition

Another most widely used, cheap and scalable way to fabricate graphene is the Chemical vapor deposition. Comparing with the other methods, this method offers high quality and large area graphene layers. In this method, a transition metal film (mostly

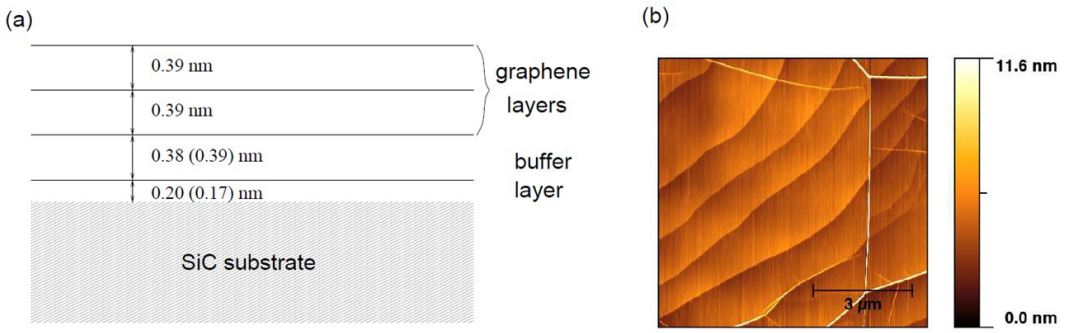

Figure 1.6. Epitaxial Graphene.(a) Schematic view for epitaxial graphene. (b) Atomic-force microscopy image of epitaxial graphene on layers of C-terminated SiC substrate (source: Jean-Noel FUCHS (2018)).

used copper(Cu)) is left in a high temperature tube (between $800^o - 1100^o$ C) to react with the gas phase C source (CH_4, C_2H_4 etc.). Thermally cracking of C atoms on the transition metal substrate produces graphene layers on substrates(1.7).

In this technique, the properties of metal substrates play the main role for high quality graphene, from the heating and cooling rates to the thickness and quality of it. If these properties are satisfied enough, CVD technique offers to produce wafer scale graphene cheaper. Due to the fact that the chemical process depends on the metal properties, single layer graphene films can be fabricated by transferring onto desired substrate, as however it is needed to use, such as on glass for optical, on Si for electronic applications. So, therefore, this method is more efficient way to produce graphene compared with the other ones (Celebi et al. (2013)).

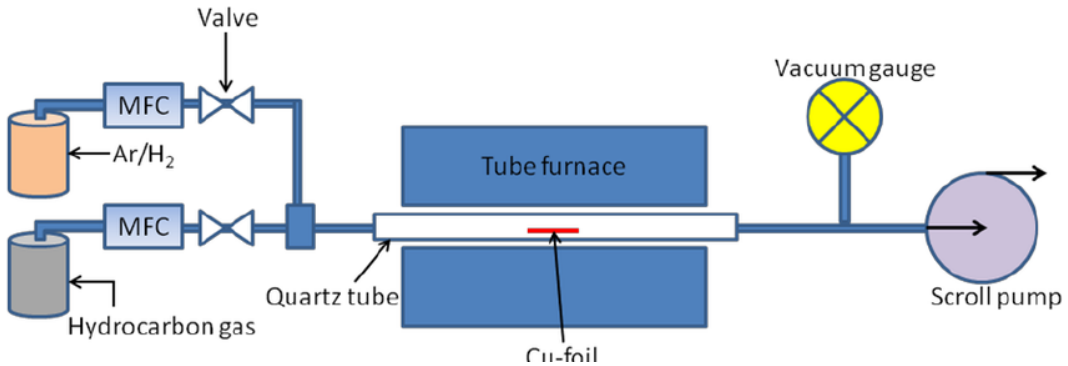

Figure 1.7. Schematic diagram of typical set-up for CVD graphene synthesis (MFC: mass flow controller)

1.4. Graphene Nanostructures and Magnetism

Despite the fact that graphene has many extraordinary properties, the electronic gapless band structure forbids graphene to be used as a field effect transistor(FET) devices or sensors. So the existence of a band gap in the electronic band structure is essential for the electronic and spintronic applications (Awschalom et al. (2013),Wolf et al. (2001),Chappert et al. (2007)). Since finite-size semi-metallic graphene is a semiconductor with an energy gap, therefore the main scientific attention began to focus on graphene nanoribbons(GNRs) , edge effects (Fujita et al. (1996), Tao et al. (2011),Magda et al. (2014)) and narrow stripes of graphene, as a promising candidate to get a bandgap for FETs (Chen et al. (2007), Han et al. (2007), Wang et al. (2008)) by introducing broken sublattice symmetry. Since the cutting breaks the sublattice symmetry, the sides of the ribbon would fit in the geometry of zigzag or armchair edges and these two different kind of edges would have different electronic properties for the ribbon. Bulk graphene does not have a band gap between the highest occupied molecular orbital(HOMO) and the lowest unoccupied molecular orbital(LUMO), and this makes the graphene useless for graphene-based device applications. However, finite ribbons have an energy gap due to breaking symmetry at the edges so that it effects the electronic properties of any graphene nanostructures, significantly (Potasz et al. (2012)), and it starts to behave as a semiconducting material. Although by cutting graphene into narrow ribbons is experimentally remains a significant challenge, recently, the production of atomically precise graphene nanoribbons with different widths has been done by using bottom-up approach (Talirz et al. (2016), Cai et al. (2010)), nevertheless, Kimouche et. al. show that ultra-narrow nanoribbons can be fabricated on Au(111) substrate (Kimouche et al. (2015),Ruffieux et al. (2016)).

On the other hand, graphene nanoribbons include band gap within Hubbard model, due to the zigzag edges of the ribbons, which have spin polarization, they consist of magnetism confirming to the Lieb's theorem (Lieb (1989)). In this case the degeneracy associated with the existence of two identical edges is slightly removed by the second neighbors hopping and interactions between the edges. Despite the fact that the perfectly pure graphene nanoribbons should have a ground state with antiferromagnetically (Fig.1.9(a)) coupled edges and with the total spin $S_z = 0$ instead of a state with ferromagnetically (Fig.1.9(b)) coupled edges. Lieb's bipartite lattice theorem for Hubbard model also predicts a finite total spin related to breaking of the sublattice symmetry (Fernández-Rossier and Palacios (2007),Son et al. (2006), Yazyev and Katsnelson (2008)). This broken symmetry can happen, for instance, at the zigzag edges of a graphene nanostructures

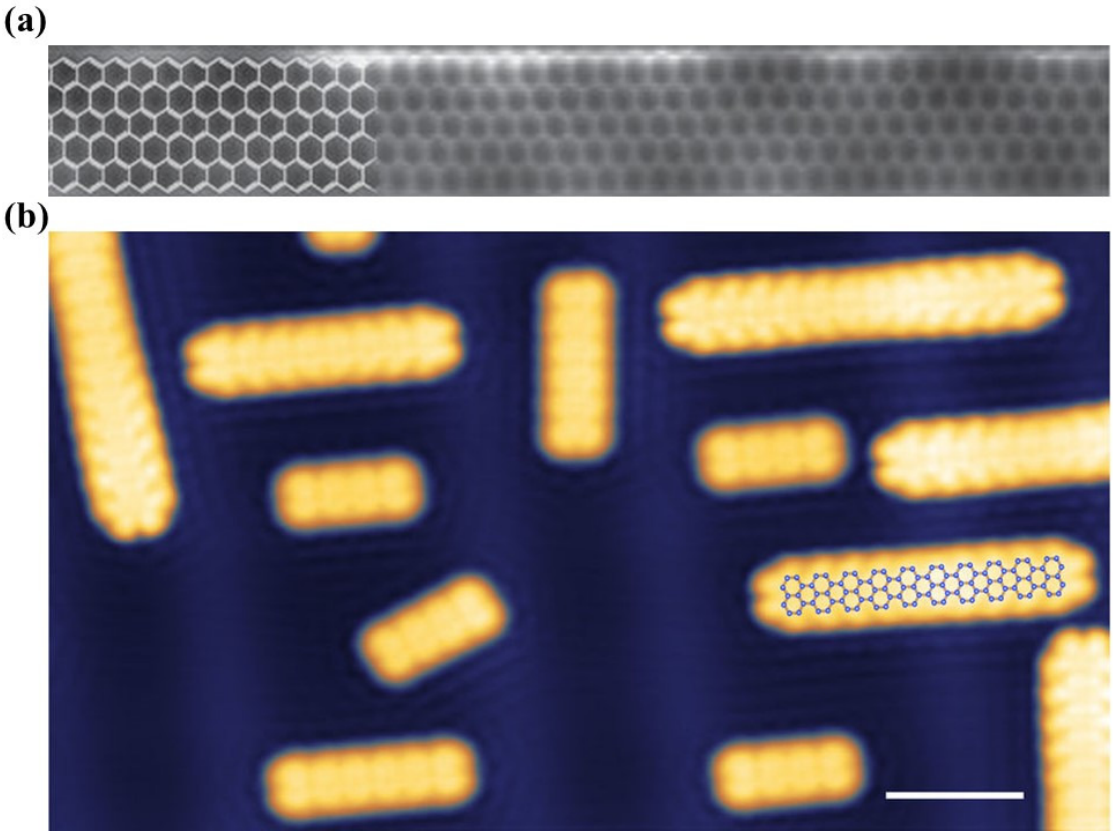

Figure 1.8. (a)The formation of a 6-ZGNR with atomically precise CH edges(Ruffieux et al. (2016)) (b) Zoomed-in STM topography of different ribbon lengths (source: Kimouche et al. (2015))

(Lee et al. (2005),Li and Lu (2008), Son et al. (2006),Cervantes-Sodi et al. (2008),Güçlü et al. (2013),Magda et al. (2014), U. Özdemir et al. (2016)) or around an atomic defect (Yazyev and Helm (2007), Palacios et al. (2008),Jaskólski et al. (2015), González-Herrero et al. (2016), Gargiulo et al. (2014),Singh and Kroll (2009), Yuanbo Zhang and Kim (2005),Pereira et al. (2008)), resulting in magnetized localized states.

It is well known that slightly above the AFM ground state energy, there is a ferromagnetic configuration (Fig.1.9(b)) with parallel spin orientation on both edges (Lee et al. (2005)). Unlike the half-filled system, AFM state might be less favourable for a disordered ZGNR. However, according to Lieb's theorem a bipartite lattice has a total spin moment proportional to the difference of the number of atoms belonging to the two sublattices (Lieb (1989)). On the other hand, Lieb's theorem does not say much about the local spin moments. So even if AFM ground state with S=0 would be the lowest energy state, local ferromagnetic order can also be seen. Most importantly, edge spin configura-

tions in zigzag ribbons makes FET transistors possible by carring spin polarized current without any external fields or lead contacts(Son et al. (2006),Vancsó et al. (2017)). Therefore, the phase transition from AFM to FM state for ZGNRs is important to realize the physical mechanism which is crucial for the proposed spintronic devices (Soriano et al. (2010),Bostwick et al. (2009),L Wang et al. (2009)). In the last year, one of our group members theoretically demonstrated that by using long-range disorder type, which is under strong potential fluctuations can induce a magnetic phase transition, in agreement with recent experimental results (U. Özdemir et al. (2016)). From this point of view, we are going to focus on the atomic disorder effects to the AFM-FM phase transition of graphene nanoribbons with zigzag edges within mean-field Hubbard approximation in this study.

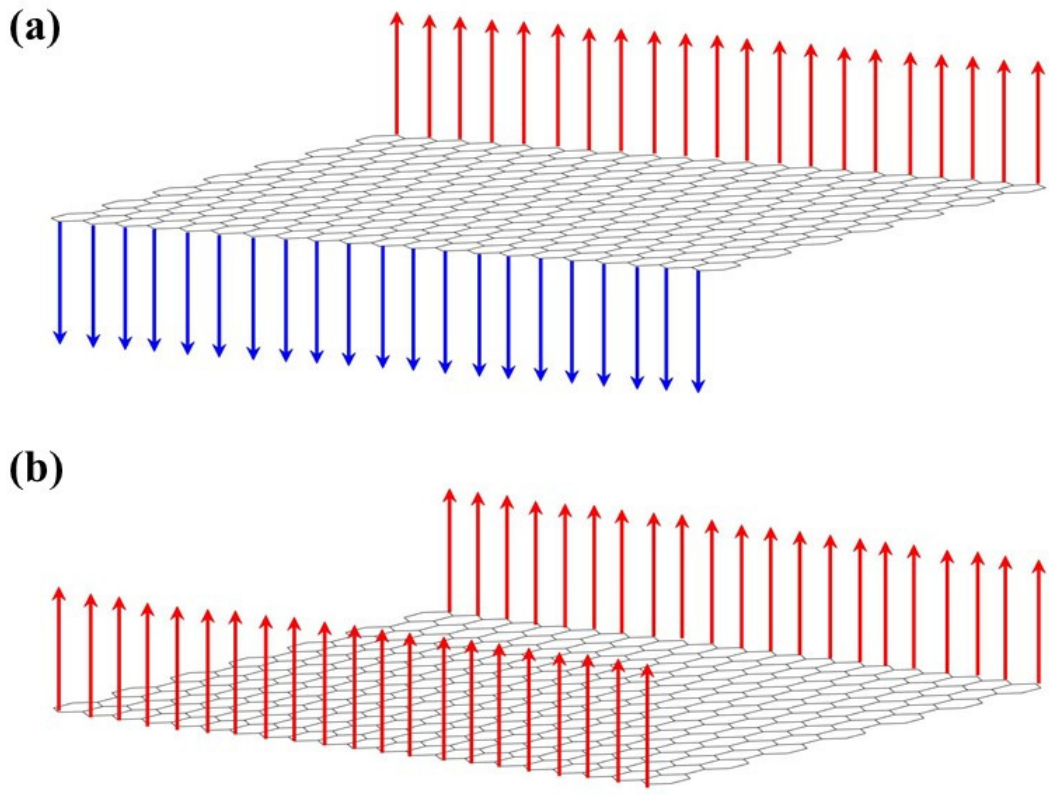

Figure 1.9. Schematic demonstration of (a) antiferromagnetically coupled and (b) ferromagnetically couppled zigzag edges in graphene nanoribbons

In this thesis, the first chapter includes the simplest graphene structure and its gradients, Carbon atom and its properties. Carbon allotropes, hybridization and graphene honeycomb lattice will be the first milestone of this work. After that, even if many other fabrication techniques exist in present, some common methods will be introduced, such as

mechanical exfoliation and epitaxial graphene. And then, a brief motivation of this study and the reasons of the interests on the nanoribbons will be demonstrated. Second chapter include all the theoretical foundations needed for this study, from tight-binding approach to the more realistic mean-field Hubbard model. By using time-dependent results, Anderson's argument will be introduced for the localization and conductivity in ZGNRs. However, there are no perfect structures, included graphene either, in nature, the source of disorders and their types will be discussed in the next chapter. In this section, short and long-range disorders will be introduced, however the main focus of this study will be related to the short-range disorder systems. Finally, after Anderson localization is theoretically explained, all the results will be given. All these results of this study are performed only for finite ZGNRs with atomic defects. Final section includes a brief summary of this study and possibilities for future work.

CHAPTER 2

THEORY AND MODELS

We start with the six electrons in the orbitals $1s^2, 2s^2$, and $2p^2$. The main contribution to the properties of graphene comes from the 4 valence electrons. There of them mainly contributes to the mechanical properties of graphene by occupying s, p_x and p_y orbitals and make sp^2 hybridization, and strong sigma bonds between the nearest neighboring carbon atoms as mentioned in previous section. The last valence electron occupies the p_z orbital orthogonal to the plane of graphene. The hybridization of p_z orbitals leads to the formation of π bonds in graphene which is responsible for the electronic properties at low energies. In this section, we will describe the single p_z orbital (π electrons) TB approximation (Wallace (1947)) and mean-field Hubbard approximation (J. (1963), Chao et al. (1977)) to investigate the electronic and magnetic properties of graphene.

2.1. Models

The honeycomb lattice is not a Bravais lattice, since two neighboring sites are not identical. In Fig.(2.1), one may view the honeycomb lattice as a triangular Bravais lattice with two-atom basis (A and B). The distance between the nearest carbon atoms is 0.142 nm, which is the average of single C-C and double C=C covalent σ bonds, as in the case of benzene.

2.1.1. Tight-Binding Model

The lattice vectors can be defined by

$$\mathbf{a}_1 = \frac{a}{2}(\sqrt{3}, 3), \mathbf{a}_2 = \frac{a}{2}(-\sqrt{3}, 3) \quad \text{and} \quad \mathbf{b} = a(0, 1) \tag{2.1}$$

Positions of all sublattice A and B atoms are given by

$$\mathbf{R}_A = n\mathbf{a}_1 + m\mathbf{a}_2 + b$$
$$\mathbf{R}_B = n\mathbf{a}_1 + m\mathbf{a}_2 \tag{2.2}$$

where n and m are integers, and b is a vector going from the A sublattice atom to the B sublattice atom in a unit cell (Fig.2.1).

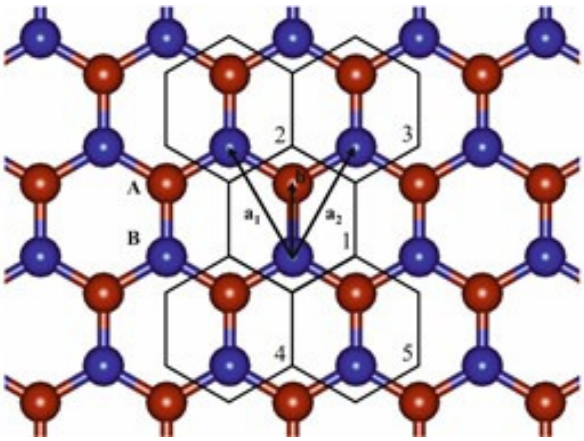

Figure 2.1. Graphene honeycomb lattice structure. The vectors $\mathbf{a}_1$, $\mathbf{a}_2$, and $\mathbf{b}$ are the primitive unit vectors connect two nearest neighboring atoms labelled with A and B separated by a distance a = 0.142 nm (reprinted from the source: Güçlü et al. (2014))

Each carbon atoms in the honeycomb lattice contributes one electron to the electronic band of state so that it is only half-filled. Fig.(2.2) illustrates this situation. Thus, we consider the tight-binding Hamiltonian to operate on the wavefunction by Schrödinger equation.

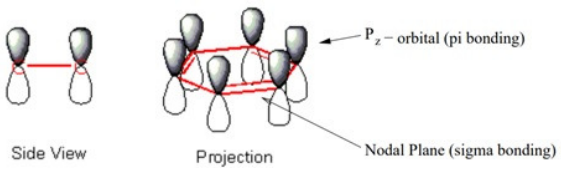

Figure 2.2. The p_z orbitals forming π bonds lie orthogonal to a nodal plane in which sigma bonding occurs.

The Hamiltonian operator has the form,

$$\hat{H} = -\frac{\hbar^2}{2m}\nabla^2 + V(\mathbf{r}), \tag{2.3}$$

where $V(\mathbf{r})$ is the potential-energy function of the electron. The wavefunction,$|\Psi\rangle$, can be written as a linear combination of all atomic orbitals (in this case the p_z orbitals) centered on each atom such that the electron wave function ψ_j for the jth atom, which are considered to be the basis vectors;

$$|\Psi\rangle = \sum_{j=1}^{N} C_j \, |\psi_j\rangle \tag{2.4}$$

Then, C_j's have to be found. Therefore, now we have to solve the time-independent Schrödinger equation,

$$\hat{H} \, |\Psi\rangle = E \, |\Psi\rangle \tag{2.5}$$

If this is multiplied from the left by $\langle\psi_i|$, it becomes

$$\sum_{j=1}^{N} C_j \big\langle \psi_i | \hat{H} | \psi_j \big\rangle = \sum_{j=1}^{N} C_j E \big\langle \psi_i | \psi_j \big\rangle, \tag{2.6}$$

and giving the simplified form,

$$\sum_{j=1}^{N} C_j \Big(\big\langle \psi_i | \hat{H} | \psi_j \big\rangle - E \big\langle \psi_i | \psi_j \big\rangle \Big) = 0 \tag{2.7}$$

If we state this summation only over the nearest neighbors atoms, the integrals in this equation can be taken as;

$$\begin{aligned} \hat{H}_{ij} = \big\langle \psi_i | \hat{H} | \psi_j \big\rangle = t, \quad & \text{if i,j are neighbors} \\ \big\langle \psi_i | \psi_j \big\rangle = \delta_{ij} & \end{aligned} \tag{2.8}$$

Here the hopping parameter, t, determines the width of the bands and the on-site energy is set to be zero. Another way apart from the atomic wavefunction is a symmetry consideration. The wavefunction must respect to the discrete translation symmetry of the lattice. Thus, one can write down the wavefunction of an electron on sublattice A and B as a linear superposition of localized p_z ortbitals of sublattice A and B, respectively, by using Bloch's theorem;

$$\psi_k^{(A)}(\mathbf{r}) = \frac{1}{\sqrt{N_A}} \sum_{R_A} e^{i\mathbf{k}\mathbf{R}_A} \psi_z(\mathbf{r} - \mathbf{R}_A)$$
$$\psi_k^{(B)}(\mathbf{r}) = \frac{1}{\sqrt{N_B}} \sum_{R_B} e^{i\mathbf{k}\mathbf{R}_B} \psi_z(\mathbf{r} - \mathbf{R}_B) \tag{2.9}$$

where the exponential part describes a symmetry operation under the physical problem is left invariant, and it also commutes with Eq.(2.3) $\left[e^{i\mathbf{k}\overrightarrow{\tau}_b}, \hat{H}\right]$=0, and where N_A,N_B are the number of A and B sublattice atoms, respectively.

After these formal considerations, in order to obtain the energy bands of graphene, we should take the particular case of the tight-binding model on the honeycomb lattice into account. Since there are several atoms in a unit cell, as in this case of honeycomb lattice, the total wavefunction as linear combination of two sublattice wavefunction can be written as,

$$\Psi_k(\mathbf{r}) = a_k \Psi_k^{(A)}(\mathbf{r}) + b_k \Psi_k^{(B)}(\mathbf{r}) \tag{2.10}$$

where a_k and b_k are complex functions of the quasi-momentum k. Now one can solve the Schrödinger Eq.(2.5) by taking the total wavefunction,and multiplying the left side by sublattice wavefunctions, seperately;

$$\hat{H} \left|\Psi_k(\mathbf{r})\right\rangle = E_k \left|\Psi_k(\mathbf{r})\right\rangle \tag{2.11}$$

One may continue in matrix form with the help of (2.9) and (2.10),

$$\begin{aligned} &\begin{pmatrix} a_k^* & b_k^* \end{pmatrix} \begin{pmatrix} \langle \psi_k^{(A)} | H | \psi_k^{(A)} \rangle & \langle \psi_k^{(A)} | H | \psi_k^{(B)} \rangle \\ \langle \psi_k^{(B)} | H | \psi_k^{(A)} \rangle & \langle \psi_k^{(B)} | H | \psi_k^{(B)} \rangle \end{pmatrix} \begin{pmatrix} a_k \\ b_k \end{pmatrix} \\ &= E_k \begin{pmatrix} a_k^* & b_k^* \end{pmatrix} \begin{pmatrix} \langle \psi_k^{(A)} | \psi_k^{(A)} \rangle & \langle \psi_k^{(A)} | \psi_k^{(B)} \rangle \\ \langle \psi_k^{(B)} | \psi_k^{(A)} \rangle & \langle \psi_k^{(B)} | \psi_k^{(B)} \rangle \end{pmatrix} \begin{pmatrix} a_k \\ b_k \end{pmatrix} \end{aligned} \tag{2.12}$$

Since the hopping parameters between the second nearest neighbors on the same sublattice and the on-site energies of p_z orbitals can be taken to be zero, the terms in this equation,

$$\begin{aligned}\left\langle \psi_k^{(A)} | H | \psi_k^{(A)} \right\rangle = \left\langle \psi_k^{(B)} | H | \psi_k^{(B)} \right\rangle \simeq 0 \\ \left\langle \psi_k^{(A)} | \psi_k^{(B)} \right\rangle = \left\langle \psi_k^{(B)} | \psi_k^{(A)} \right\rangle = 0\end{aligned} \tag{2.13}$$

Now, the problem reduced to solve just off-diagonal $\left\langle \psi_k^{(B)} | H | \psi_k^{(A)} \right\rangle$ terms in the Hamiltonian, as the following

$$\begin{aligned}< \psi_k^{(B)} | H | \psi_k^{(A)} >= & \frac{1}{N} \sum_{\mathbf{R}_A, \mathbf{R}_B} e^{i(\mathbf{R}_A - \mathbf{R}_B)} \\ & \int d\mathbf{r} \psi_z^*(\mathbf{r} - \mathbf{R}_B) V(\mathbf{r} - \mathbf{R}_B) \psi_z(\mathbf{r} - \mathbf{R}_A)\end{aligned} \tag{2.14}$$

Since the integral of this equation is constant for a given pair of nearest neighbors at R_A and R_B, one may write down by using Eq.(2.1) and R_A,R_B in Eq.(2.2),

$$\begin{aligned}< \psi_k^{(B)} | H | \psi_k^{(A)} >= t(e^{-i\mathbf{kb}} + e^{-i\mathbf{k}(\mathbf{b}-\mathbf{a}_1)} + e^{-i\mathbf{k}(\mathbf{b}-\mathbf{a}_2)}) \\ < \psi_k^{(A)} | H | \psi_k^{(B)} >= t(e^{i\mathbf{kb}} + e^{i\mathbf{k}(\mathbf{b}-\mathbf{a}_1)} + e^{i\mathbf{k}(\mathbf{b}-\mathbf{a}_2)})\end{aligned} \tag{2.15}$$

The hopping amplitude between nearest neighbors is given by the expression,

$$t_{nn} = \int d\mathbf{r} \psi_z^*(\mathbf{r} - \mathbf{R}_B) V(\mathbf{r} - \mathbf{R}_B) \psi_z(\mathbf{r} - \mathbf{R}_A) \tag{2.16}$$

and this parameter is usually taken $t_{nn} = 2.8$ eV and the second nearest neighbor parameter is similar to Eq.(2.16) and taken as $t_{nnn} = 0.1$ eV (Castro Neto et al. (2009)). Eventually, we can solve the Schrödinger equation now to find the energy band diagram of the graphene. By defining,

$$f(\mathbf{k}) = e^{-i\mathbf{kb}} + e^{-i\mathbf{k}(\mathbf{b}-\mathbf{a}_1)} + e^{-i\mathbf{k}(\mathbf{b}-\mathbf{a}_2)} \tag{2.17}$$

The eigenvalue problem in matrix notation,

$$E \begin{pmatrix} a_k \\ b_k \end{pmatrix} = t \begin{pmatrix} 0 & f(\mathbf{k}) \\ f^*(\mathbf{k}) & 0 \end{pmatrix} \begin{pmatrix} a_k \\ b_k \end{pmatrix} \tag{2.18}$$

And its solutions are,

$$E_{\pm}(\mathbf{k}) = \pm \left| t f(\mathbf{k}) \right| \tag{2.19}$$

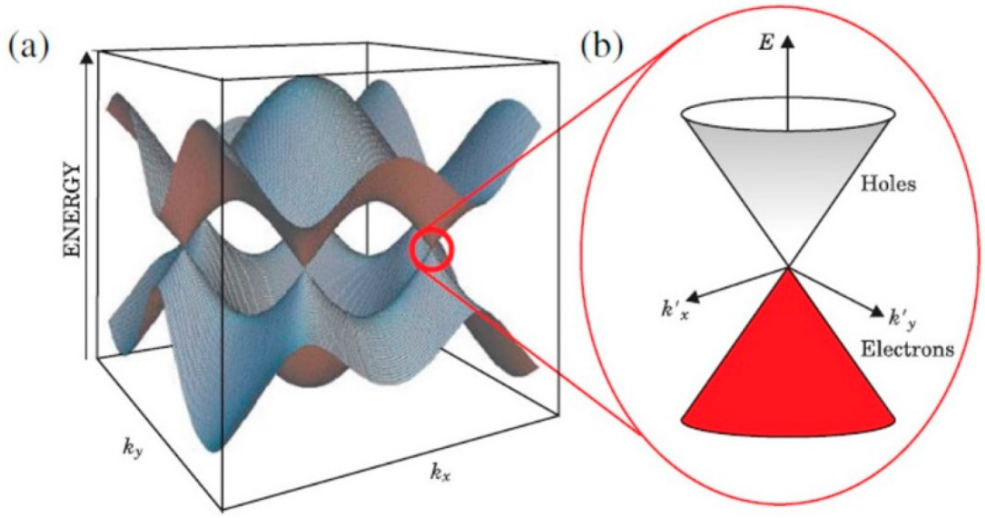

Figure 2.3. (a) Graphene band structure. (b) A schematic representation of a Dirac cone and the meeting of the conduction band and valence band close to the K and K'. Adapted from (source: Das Sarma et al. (2011))

Note that the spectrum is gapless at six K points due to the properties of Dirac fermions and there is a symmetry with respect to the Fermi level (E_{Fermi}=0). However this symmetry is broken if the next nearest neighbors are taken into account. For the constant a_k and b_k in Eq.(2.10) and Eq.(2.18),

$$\begin{pmatrix} a_k \\ b_k \end{pmatrix} = \frac{1}{\sqrt{2}} \begin{pmatrix} 1 \\ \frac{\pm f^*(\mathbf{k})}{\left| f(\mathbf{k}) \right|} \end{pmatrix} \tag{2.20}$$

This result holds only for the bulk graphene (for 2D) to find conduction and valence band wavefunctions in k-space. However, a finite ZGNR system in the real space offers not only controlling each atoms and the atomic disorders in the system but also optimizing it easier. Therefore, we have made our calculations in real space for the finite zigzag graphene nanoribbons(ZGNRs) . In the next subsection, we will introduce the edge effects in graphene nanoribbons and the numerical method which we used for tight-binding method.

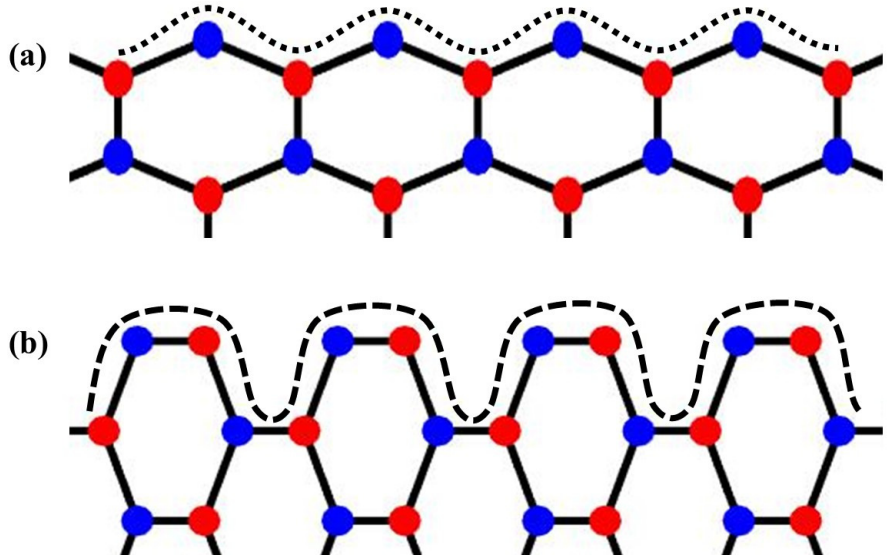

Figure 2.4. Two different edge geometry:(a) zigzag edges (b) armchair edges for a graphene nanoribbon.

2.1.2. Edge Effects in Graphene Nanoribbons

We have considered the one-band empirical tight-binding model introduced by Wallace (Wallace (1947)) and demonstrated the one-electron spectrum for a bulk graphene in the previous subsection. Now, we can discuss about the application of TB model to GNRs. The TB Hamiltonian in terms of p_z orbitals localized on each carbon atoms in the simplest way can be introduced by using annihilation and creation operators,

$$H_{TB} = t \sum_{<i,j>,\sigma} c^*_{i\sigma} c_{j\sigma} \tag{2.21}$$

where $< i, j >$ indicates a summation over only nearest neighbor sites. $c_{i\sigma}$ and $c^*_{i\sigma}$ are creation and annihilation operators for an electron on the lattice site i with spin σ. We can describe the effective Hamiltonian by using the same methodology by cutting the bulk graphene. If the most appropriate geometric cutting would be used, then there can be created two separate kind of nanoribbons with zigzag and armchair edges as in Fig.(2.4).

The TB Hamiltonian for finite-size systems can be described by limiting the matrix elements to the atoms in the graphene nanoribbon. We consider now, a method of constructing the TB Hamiltonian matrix as an example of a ribbon with zigzag edges,

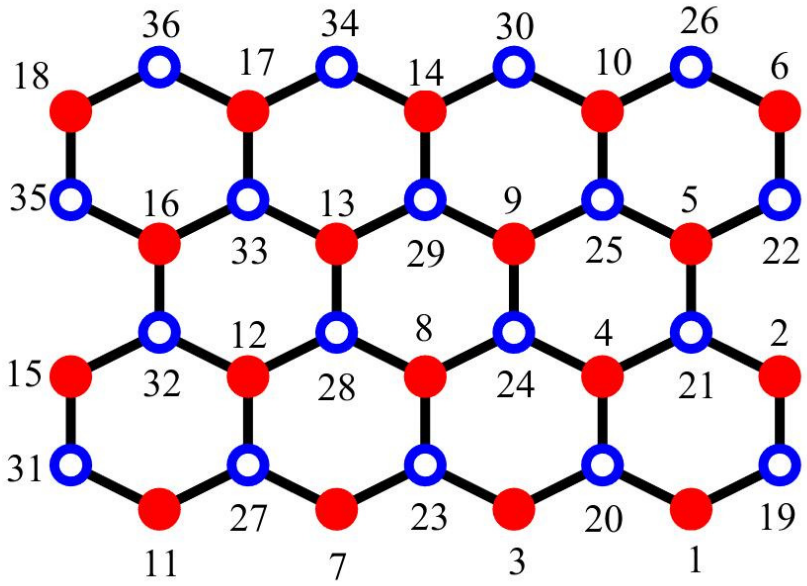

Figure 2.5. Example of a zigzag graphene nanoribbon with N=36 atoms.

shown in Fig.(2.5), includes of 18 A and 18 B atoms, totally of $N = 36$ atoms. In the figure, you can see that the edge atoms have two nearest neighbors instead of three in the bulk case. The locations of all sublattice atoms in the ribbon are given by the R_A and R_B vectors in Eq.(2.2), where n and m are integers. These n and m integers are describing the position of all sublattice atoms instead of i and j indices as shown in Fig.(2.5). By only keeping the nearest neighbor hopping parameter (tunneling matrix element) in the TB Hamiltonian, the other matrix elements are all zero. For instances, the carbon atom 1 has a sigma bond with 20 and 19. Therefore, the first row of the TB Hamiltonian matrix includes all zeros except for 19th and 20th columns, which we have t. All other rows can be constructed in a similar way. Once the Hamiltonian is built, it may be diagonalized numerically yielding eigenvalues and eigenvectors labeled by indices (for N atoms) as in Eq.(2.22).

Constructing and diagonalizing the Hamiltonian in this way is numerically giving the eigenvalues and eigenfunctions corresponding to the labeled indices. The energy spectrums of different sample of systems are shown in the Fig.(2.6). One can state that the ribbon width makes the system metallic or semiconducting. In the Fig.(2.6(a)), the system has no zero energy states, also known as "edge states" which are expected to be

localized at the zigzag edges. However when we increase the number of atoms in the system along the zigzag edges, we get more edge states at the Fermi level. Hence, we can consider these localized states are related to the electrons moving at the edges, the size of the samples effects and closes the energy gap more quickly for longer ribbon.

$$H_{TB} = \begin{bmatrix} 0 & t & 0 & 0 & 0 & \dots & t \\ t & 0 & t & 0 & 0 & \dots & 0 \\ 0 & t & 0 & t & 0 & \dots & 0 \\ 0 & 0 & t & 0 & t & \dots & 0 \\ 0 & 0 & 0 & t & 0 & \ddots & \vdots \\ \vdots & \vdots & \vdots & \vdots & \ddots & \ddots & t \\ t & 0 & 0 & 0 & \dots & t & 0 \end{bmatrix}_{N \times N} \tag{2.22}$$

This numerically effective Hamiltonian has been considered in our all calculations and there are no calculations in armchair graphene nanoribbons in this study. Next subchapter, we will discuss the mean-field Hubbard model for the electron-electron interactions.

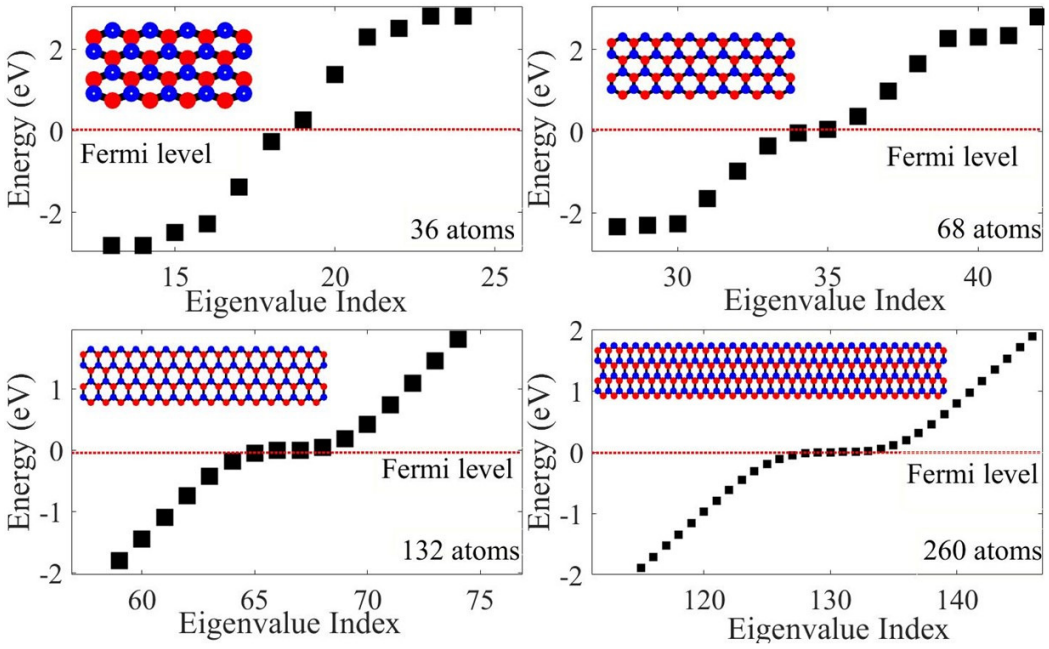

Figure 2.6. TB energy spectra consisting degenerate states at Fermi level for graphene quantum dots to graphene nanoribbons by increasing the number of atoms horizontally as (a) 36 atoms, (b) 68 atoms, (c)132 atoms, (d)260 atoms.

2.1.3. Mean-Field Hubbard Model

The Hubbard model gives us a chance to understand how the interactions between electrons can get the material to insulating, magnetic and even novel superconducting. The Hubbard model has been studied by condensed matter theorists from mean field approaches to the theoretical methods employing Feynman diagrams, expansions in the degeneracy of the number of spin, angular momentum, etc. It has been used with numerical methods like diagonalization and quantum Monte Carlo, as well.

Mean field Hubbard approach is applied to determine the ground-state properties. Tight-binding model has no information about magnetism, spin dependency and electron-electron interactions in ZGNRs. The purpose of this part in this section is to provide a basic explanation to the Hubbard model. So, one can start to the Hamiltonian of interacting electrons by solving many-body problem. However, only very small systems can be exactly solvable with a good approximation. Therefore, one can reduce this problem to one-body problem by introducing the "background nuclei potential field" in which each electron is moving. Since we are mainly interested in valance electrons or p_z electrons only.

Beginning with the many-body Hamiltonian in second quantization and expanding the field operators in terms of basis states and creation (annihilation) operators, which proves the antisymmetry of many-body states, we can derive the mean-field Hubbard Hamiltonian as,

$$H = \sum_{pq} \hat{t}_{pq} c_p^\dagger c_q + \frac{1}{2} \sum_{pqrs} \langle pq|\hat{V}|rs\rangle c_p^\dagger c_q^\dagger c_r c_s \tag{2.23}$$

while $\hat{t}$ and $\hat{V}$ are spin independent, the terms p, q, r and s are states in order to show the spin dependency defined as $p = i\sigma$, $q = j\sigma^{'}$, $r = k\sigma^{''}$ and $s = l\sigma^{'''}$. These make the first and second (interaction) terms in the Eq.(2.23),

$$\begin{aligned}
\hat{t}_{pq} &= \langle p|t|q\rangle = \langle i\sigma|t|j\sigma^{'}\rangle = \langle i|t|j\rangle \underbrace{\langle \sigma|\sigma_{'}\rangle}_{\delta_{\sigma\sigma'}} = t_{ij}\delta_{\sigma\sigma'} \\
\hat{V}_{pqrs} &= \langle pq|\hat{V}|rs\rangle = \langle i\sigma|\langle j\sigma^{'}|\hat{V}|k\sigma^{''}\rangle|l\sigma^{'''}\rangle = \langle i|\langle j|\hat{V}|k\rangle|l\rangle \underbrace{\langle \sigma|\underbrace{\langle \sigma^{'}|\sigma^{''}\rangle}_{\delta_{\sigma^{'}\sigma^{''}}}|\sigma^{'''}\rangle}_{\delta_{\sigma\sigma^{'''}}} \\
&= \hat{V}_{ijkl}\delta_{\sigma^{'}\sigma^{''}}\delta_{\sigma\sigma^{'''}}
\end{aligned} \tag{2.24}$$

Then the Hamiltonian in Eq.(2.23) becomes,

$$H = \sum_{\substack{<i,j> \\ \sigma}} \hat{t}_{ij} c^{\dagger}_{i\sigma} c_{j\sigma} + \frac{1}{2} \sum_{\substack{ijkl \\ \sigma\sigma^{'}}} \left\langle ij|\hat{V}|kl \right\rangle c^{\dagger}_{i\sigma} c^{\dagger}_{j\sigma^{'}} c_{k\sigma^{'}} c_{l\sigma} \tag{2.25}$$

with the Coulomb matrix elements,

$$\left\langle ij|\hat{V}|kl \right\rangle = \int\int d\mathbf{r}_1 d\mathbf{r}_2 \psi^{\star}_i(\mathbf{r}_1)\psi^{\star}_j(\mathbf{r}_2)\frac{2}{\kappa|\mathbf{r}_2 - \mathbf{r}_1|}\psi_k(\mathbf{r}_2)\psi_l(\mathbf{r}_1) \tag{2.26}$$

and $\mathbf{r}_1$ and $\mathbf{r}_2$ are coordinates of the two different electrons. Hear we note that if $l = i$ and $k = j$, the second term, $\left\langle ij|\hat{V}|kl \right\rangle$, corresponds to the Coulomb interaction between two electronic densities localized on sites i and j. Also the other option, $\left\langle ij|\hat{V}|kl \right\rangle$ for $l = j$ and $k = i$, is for the exchange term which comes along only if electrons on i and j orbitals have the same spin $\sigma = \sigma^{'}$ in Eq.(2.25). Therefore, if we only keep the terms of interaction matrix as non-zero terms,

$$\begin{aligned} &\left\langle ii|\hat{V}|ii \right\rangle = U \qquad \text{and} \\ &\left\langle ji|\hat{V}|ij \right\rangle = \hat{V}_{ij} \end{aligned} \tag{2.27}$$

and the other terms will be assumed as zero matrix elements. So we have two different non-zero terms in the interaction matrix in Eq.(2.24), when $i = j = k = l$, first term the diagonal term can be written as,

$$\sum_{\substack{ijkl \\ \sigma\sigma^{'}}} \left\langle ij|\hat{V}|kl \right\rangle c^{\dagger}_{i\sigma} c^{\dagger}_{j\sigma^{'}} c_{k\sigma^{'}} c_{l\sigma} \rightarrow U \sum_{\substack{i \\ \sigma\neq\sigma^{'}}} c^{\dagger}_{i\sigma} c^{\dagger}_{i\sigma^{'}} c_{i\sigma^{'}} c_{i\sigma} \tag{2.28}$$

Since $\sigma \neq \sigma^{'}$ due to the Pauli-exclusion principle and also, we assumed as they are different initially. Then, by using the anticommutation relations,

$$\begin{aligned} \{c_{i\sigma^{'}}, c_{i\sigma}\} = 0 \qquad &\text{since} \quad \sigma \neq \sigma^{'} \\ c_{i\sigma^{'}} c_{i\sigma} = -c_{i\sigma} c_{i\sigma^{'}} \end{aligned} \tag{2.29}$$

This makes the Eq.(2.28) as,

$$U \sum_{\substack{i \\ \sigma\neq\sigma^{'}}} c^{\dagger}_{i\sigma} c^{\dagger}_{i\sigma^{'}} c_{i\sigma^{'}} c_{i\sigma} \rightarrow -U \sum_{\substack{i \\ \sigma\neq\sigma^{'}}} c^{\dagger}_{i\sigma} c^{\dagger}_{i\sigma^{'}} c_{i\sigma} c_{i\sigma^{'}} \tag{2.30}$$

And, we can use the commutation relation,

$$\begin{aligned} \{c^{\dagger}_{i\sigma'}, c_{i\sigma}\} &= 0 \\ c^{\dagger}_{i\sigma'} c_{i\sigma} &= -c_{i\sigma} c^{\dagger}_{i\sigma'} \end{aligned} \tag{2.31}$$

Thus, we can introduce the number operators $n_{i\sigma} = c^{\dagger}_{i\sigma} c_{i\sigma}$ and Eq.(2.30) becomes;

$$-U \sum_{\substack{i \\ \sigma \neq \sigma'}} c^{\dagger}_{i\sigma} c^{\dagger}_{i\sigma'} c_{i\sigma} c_{i\sigma'} \rightarrow U \sum_{\substack{i \\ \sigma \neq \sigma'}} \underbrace{c^{\dagger}_{i\sigma} c_{i\sigma}}_{n_{i\sigma}} \underbrace{c^{\dagger}_{i\sigma'} c_{i\sigma'}}_{n_{i\sigma'}} \tag{2.32}$$

On the other hand, the $\langle ij|\hat{V}|kl\rangle$ matrix includes other non-zero elements, similarly for $k = l$ and $l = i$,

$$\sum_{\substack{ijkl \\ \sigma\sigma'}} \langle ij|\hat{V}|kl\rangle c^{\dagger}_{i\sigma} c^{\dagger}_{j\sigma'} c_{k\sigma'} c_{l\sigma} \rightarrow \sum_{\substack{ij \\ \sigma\sigma'}} \hat{V}_{ij} c^{\dagger}_{i\sigma} c^{\dagger}_{j\sigma'} c_{j\sigma'} c_{i\sigma} \tag{2.33}$$

and by using the commutation relations,

$$\begin{aligned} \{c_{j\sigma'}, c_{i\sigma}\} = 0 \rightarrow c_{j\sigma'} c_{i\sigma} &= -c_{i\sigma} c_{j\sigma'} \quad \text{and} \\ \{c^{\dagger}_{j\sigma'}, c_{i\sigma}\} = 0 \rightarrow c^{\dagger}_{j\sigma'} c_{i\sigma} &= -c_{i\sigma} c^{\dagger}_{j\sigma'} \end{aligned} \tag{2.34}$$

And then Eq.(2.33) becomes,

$$\begin{aligned} \sum_{\substack{ij \\ \sigma\sigma'}} \hat{V}_{ij} c^{\dagger}_{i\sigma} c^{\dagger}_{j\sigma'} c_{j\sigma'} c_{i\sigma} &\rightarrow -\sum_{\substack{ij \\ \sigma\sigma'}} \hat{V}_{ij} c^{\dagger}_{i\sigma} c^{\dagger}_{j\sigma'} c_{i\sigma} c_{j\sigma'} \\ -\sum_{\substack{ij \\ \sigma\sigma'}} \hat{V}_{ij} c^{\dagger}_{i\sigma} c^{\dagger}_{j\sigma'} c_{i\sigma} c_{j\sigma'} \rightarrow \sum_{\substack{ij \\ \sigma\sigma'}} \hat{V}_{ij} \underbrace{c^{\dagger}_{i\sigma} c_{i\sigma}}_{n_{i\sigma}} \underbrace{c^{\dagger}_{j\sigma'} c_{j\sigma'}}_{n_{j\sigma'}} &= \sum_{\substack{ij \\ \sigma\sigma'}} \hat{V}_{ij} n_{i\sigma} n_{j\sigma'} \end{aligned} \tag{2.35}$$

Eventually, the Hamiltonian now with the Eq.(2.32) and Eq.(2.34),

$$H = \sum_{\substack{<i,j> \\ \sigma}} \hat{t}_{ij} c^{\dagger}_{i\sigma} c_{j\sigma} + \frac{1}{2} \Big\{ \underbrace{U \sum_{\substack{i \\ \sigma\sigma'}} n_{i\sigma} n_{i\sigma'}}_{\text{term 1}} + \underbrace{\sum_{\substack{ij \\ \sigma\sigma'}} \hat{V}_{ij} n_{i\sigma} n_{j\sigma'}}_{\text{term 2}} \Big\} \tag{2.36}$$

Term 1-2 have 2 and 4 different spin configurations, respectively. In the term-1 , we have $\sigma = \uparrow, \sigma' = \downarrow$ or $\sigma = \downarrow, \sigma' = \uparrow$ configurations. Therefore,

$$U\sum_{\substack{i\\ \sigma\sigma^{'}}} n_{i\sigma}n_{i\sigma^{'}} \rightarrow U\sum_{i}\{n_{i\uparrow}n_{i\downarrow}+n_{i\downarrow}n_{i\uparrow}\} = 2U\sum_{i} n_{i\uparrow}n_{i\downarrow} \tag{2.37}$$

Also, in the term-2, we have 4 possible spin configurations such as, $\sigma =\uparrow$,$\sigma^{'} =\uparrow$, $\sigma =\uparrow$,$\sigma^{'} =\downarrow$, $\sigma =\downarrow$,$\sigma^{'} =\uparrow$ and $\sigma =\downarrow$,$\sigma^{'} =\downarrow$. Thus;

$$\sum_{\substack{ij\\ \sigma\sigma^{'}}} \hat{V}_{ij}n_{i\sigma}n_{j\sigma^{'}} \rightarrow \sum_{\substack{ij\\ \sigma\sigma^{'}}} \hat{V}_{ij}\{\underbrace{n_{i\uparrow}n_{j\uparrow}+n_{i\uparrow}n_{j\downarrow}+n_{i\downarrow}n_{j\uparrow}+n_{i\downarrow}n_{j\downarrow}}_{\underbrace{(n_{i\uparrow}+n_{i\downarrow})}_{n_i}\underbrace{(n_{j\uparrow}+n_{j\downarrow})}_{n_j}}\} \tag{2.38}$$

Then, the final form of the Hamiltonian in Eq. (2.36) becomes now,

$$H = \underbrace{\underbrace{\sum_{\substack{<i,j>\\ \sigma}} \hat{t}_{ij}c^{\dagger}_{i\sigma}c_{j\sigma} + U\sum_{i} n_{i\uparrow}n_{i\downarrow}}_{\text{Hubbard Model}} + \frac{1}{2}\sum_{\substack{ij\\ \sigma\sigma^{'}}} \hat{V}_{ij}n_in_j}_{\text{Extended Hubbard Model}} \tag{2.39}$$

This is the exact Hubbard Hamiltonian, and we should find now the mean-field Hubbard Hamiltonian. We start with defining these;

$$\begin{aligned} n_{i\uparrow} &= \langle n_{i\uparrow}\rangle + \underbrace{(n_{i\uparrow} - \langle n_{i\uparrow}\rangle)}_{\triangle n_{i\uparrow}} \\ n_{i\downarrow} &= \langle n_{i\downarrow}\rangle + \underbrace{(n_{i\downarrow} - \langle n_{i\downarrow}\rangle)}_{\triangle n_{i\downarrow}} \end{aligned} \tag{2.40}$$

And putting these terms into the Hubbard interaction terms and assuming $\triangle n_{i\sigma}$ terms are really small;

$$\begin{aligned} n_{i\uparrow}n_{i\downarrow} &= \left[\langle n_{i\uparrow}\rangle + (n_{i\uparrow} - \langle n_{i\uparrow}\rangle)\right]\left[\langle n_{i\downarrow}\rangle + (n_{i\downarrow} - \langle n_{i\downarrow}\rangle)\right] \\ &\approx \langle n_{i\uparrow}\rangle\langle n_{i\downarrow}\rangle + \langle n_{i\uparrow}\rangle(n_{i\downarrow} - \langle n_{i\downarrow}\rangle) + \langle n_{i\downarrow}\rangle(n_{i\uparrow} - \langle n_{i\uparrow}\rangle) \\ &= n_{i\uparrow}\langle n_{i\downarrow}\rangle + n_{i\downarrow}\langle n_{i\uparrow}\rangle - \langle n_{i\uparrow}\rangle\langle n_{i\downarrow}\rangle \end{aligned} \tag{2.41}$$

We ignored the $\triangle n_{i\uparrow} \triangle n_{i\downarrow}$ term since it is too small. Also, the other term will become,

$$n_in_j = n_i\langle n_j\rangle + n_j\langle n_i\rangle - \langle n_i\rangle\langle n_j\rangle \tag{2.42}$$

Therefore; by using Eq.(2.41) and Eq.(2.42) the mean-field Hubbard Hamiltonian becomes,

$$\begin{aligned} H \approx H_{MF} = &\sum_{\substack{<i,j> \\ \sigma}} \hat{t}_{ij} c_{i\sigma}^{\dagger} c_{j\sigma} + U \sum_{i} (n_{i\uparrow} \langle n_{i\downarrow} \rangle + n_{i\downarrow} \langle n_{i\uparrow} \rangle - \langle n_{i\uparrow} \rangle \langle n_{i\downarrow} \rangle) \\ &+ \frac{1}{2} \sum_{\substack{ij \\ \sigma\sigma'}} \hat{V}_{ij} (n_i \langle n_j \rangle + n_j \langle n_i \rangle - \langle n_i \rangle \langle n_j \rangle) \end{aligned} \tag{2.43}$$

However, this is something important within this equation now due to the $\hat{t}_{ij}$ part. All terms in this equation are now quadratic in terms of "$c_{i\sigma}^{\dagger} c_{j\sigma}$". Thus, we can take this Hamiltonian as;

$$H_{MF} \rightarrow H_{MF}^{Bulk} = \sum_{ij\sigma} \hat{\tau}_{ij} c_{i\sigma}^{\dagger} c_{j\sigma} \tag{2.44}$$

Now we can assume for a bulk structure that;

$$\begin{aligned} \langle n_i \rangle &\equiv 1 \\ \langle n_{i\sigma} \rangle &\equiv \frac{1}{2} \end{aligned} \tag{2.45}$$

So, the following equation must be satisfied;

$$\begin{aligned} H_{MF} &= H_{MF} - H_{MF}^{Bulk} + H_{MF}^{Bulk} \\ &= \cancelto{0}{\sum_{\substack{<i,j> \\ \sigma}} \hat{t}_{ij} c_{i\sigma}^{\dagger} c_{j\sigma}} + U \sum_{i} n_{i\uparrow} n_{i\downarrow} + \frac{1}{2} \sum_{\substack{ij \\ \sigma\sigma'}} \hat{V}_{ij} n_i n_j \\ &- \cancelto{0}{\sum_{\substack{<i,j> \\ \sigma}} \hat{t}_{ij} c_{i\sigma}^{\dagger} c_{j\sigma}} - \frac{U}{2} \sum_{i} (n_{i\uparrow} + n_{i\downarrow} - \frac{1}{2}) - \frac{1}{2} \sum_{\substack{ij \\ \sigma\sigma'}} \hat{V}_{ij} (n_i + n_j - 1) \\ &+ \sum_{ij\sigma} \hat{\tau}_{ij} c_{i\sigma}^{\dagger} c_{j\sigma} \end{aligned} \tag{2.46}$$

this must be equal to;

$$H_{MF} = \sum_{ij\sigma} \hat{\tau}_{ij} c^{\dagger}_{i\sigma} c_{j\sigma} + U \sum_{i} \left[n_{i\downarrow} (\langle n_{i\uparrow} \rangle - \frac{1}{2}) + n_{i\uparrow} (\langle n_{i\downarrow} \rangle - \frac{1}{2}) \right] + \frac{1}{2} \sum_{\substack{ij \\ \sigma\sigma'}} \hat{V}_{ij} \left[(\langle n_i \rangle - 1) n_j + (\langle n_j \rangle - 1) n_i \right] \tag{2.47}$$

Since we know $\hat{V}_{ij} = \hat{V}_{ji}$ or $(\langle n_i \rangle - 1) n_j = (\langle n_j \rangle - 1) n_i$ can be taken, the last form of the mean field Hubbard Hamiltonian will become,

$$H_{MFH} = \sum_{ij\sigma} \hat{\tau}_{ij} c^{\dagger}_{i\sigma} c_{j\sigma} + U \sum_{i} \left[n_{i\downarrow} (\langle n_{i\uparrow} \rangle - \frac{1}{2}) + n_{i\uparrow} (\langle n_{i\downarrow} \rangle - \frac{1}{2}) \right] + \sum_{\substack{ij \\ \sigma\sigma'}} \hat{V}_{ij} \left[(\langle n_i \rangle - 1) n_j \right] \tag{2.48}$$

Since this final Hamiltonian does not include any quadratic terms in $c_{j\sigma}$, the problem has a quartic form, now. However, since we don't know the average occupation numbers in the Hamiltonian, one can begin with using some initial density matrices to calculate, numerically. In the similar manner by TB effective Hamiltonian, by using the n and m integers in R_A and R_B vectors, one can find the total Hamiltonian consisting the electron-electron interactions by adding U and V_{ij} terms into the TB Hamiltonian in Eq.(2.22). Next subchapter, we will discuss the disorder classifications and we will give some fundamental description for them to introduce our concept.

2.2. Disorder in Graphene

In condensed matter physics, magnetism is traditionally supposed to be in solids due to the partially filled d and f shells. Also, carbon atoms do not have magnetic moments, themselves. Therefore, the researchers working on graphene spintronics mainly scope to the significant magnetism in graphene. The induced magnetism behaviour is predicted by several theoretical models, including density functional theory (DFT) (Son et al. (2006),Singh and Kroll (2009), Soriano et al. (2010),Lee et al. (2005)), the mean-field approximation of Hubbard model (Fujita et al. (1996),Yazyev (2008),U. Özdemir et al. (2016), Yazyev (2010),Jung and MacDonald (2009),Palacios et al. (2008)), exact diagonalization (Güçlü et al. (2009),Modarresi and Güçlü (2017)) and quantum Monte Carlo simulation (Feldner et al. (2010)). However, on the experimental side, the direct

observation of magnetism in graphene nanoribbons is still lacking, most likely due to limited control over edge structure. Recently, a semiconductor-to-metal transition as a function of ribbon width was observed in nanotailored graphene ribbons with zigzag edges (Magda et al. (2014)), attributed to a magnetic phase transition from the antiferromagnetic(AFM) configuration to the ferromagnetic(FM) configuration, raising hopes for the fabrication of graphene-based spintronic and magnetic storage devices. Possible theoretical explanations for the observed AFM to FM transition in ZGNR include doping (Schubert and Fehske (2012),Topsakal et al. (2008),Dai Q.Q. and Jiang (2013)) and formation of electron-hole puddles through long range Coulomb impurities (U. Özdemir et al. (2016)).

So far, we considered all the theoretical approaches into our calculations with perfectly clean structures. However, structural or environmental disorders should be considered, since the opposite, "perfectly clean material" does not occurs in nature in order to provide graphene-based devices. For instance; the graphene field effect transistors need to be placed on substrates, or the p_z electrons can be occupied by different atoms in the atmosphere. These disorder types can be considered into two main concepts as long-range and short-range disorders.

2.2.1. Long-range Disorder

Graphene nanoribbon on a substrate can be disordered due to the surface atoms of the substrate, and we take these as a long-range disorder. In this disorder character, substrate has electron-hole puddles which can cover a portion of the nanoribbon in the scale of nm (Gibertini et al. (2012)). Due to this electron-hole puddles, the p_z electrons are effected and they are localized at some points in the nanoribbon. The ribbon has this type of pattern through itself reduces the conductivity due to its different chemical potentials.

In order to model the long-range disorder due to the potential fluctuations by the substrate, we can use a superposition of gaussian electrostatic potential V_{imp}, can be written as;

$$V_{imp}(i) = \sum_n V_n e^{-\frac{(\mathbf{r}_i - \mathbf{r}_n)}{2\sigma^2}} \tag{2.49}$$

where V_n can be chosen as a parameter in terms of hopping parameter, and σ is the width

of the potential. The long-range disorders can cause a magnetic phase transition and since the main subject of this thesis is the short-range disorder type, one can find the results in the Refr. (U. Özdemir et al. (2016)). With the limits of $\sigma \rightarrow 0$ and $V_n \rightarrow \infty$ leads to short-range disorder scenario(Schubert and Fehske (2008)).

2.2.2. Short-range Disorder

Short-range disorder includes vacancies, hydrogenation, adsorption, lattice defects, etc. In this type of disorder, one can see the local magnetic moments on the ZGNRs particularly in the vicinity of the defect sites. However, this does not mean the ribbon can be magnetized globally. The lattice defects are capable of breaking the lattice symmetry in the honeycomb lattice. This broken symmetry causes a sharply local magnetic moment around the defect site. Therefore, locally, one can induce a magnetism in ribbon by introducing the lattice defects. Atomic defects have a significant influence on the magnetic properties of graphene, as was shown before in several theoretical work (Yazyev and Helm (2007),Palacios et al. (2008), Jaskólski et al. (2015),González-Herrero et al. (2016),Gargiulo et al. (2014), Esquinazi et al. (2003),Soriano et al. (2010),Güçlü and Bulut (2015),Zhang et al. (2016)). Recently, the existence of magnetism in graphene by using hydrogen atoms was observed (González-Herrero et al. (2016)) and another direct experimental evidence of the magnetism in graphene due to single atomic vacancy in graphene was detected by using scanning tunneling microscope (Zhang et al. (2016)). An open question is the effect of the induced magnetic moment by a random distribution of atomic defects on the stability of the antiferromagnetic phase of ZGNR.

As a starting point, a vacancy can be introduced as a missing atom in the ribbon or as a hydrogenated p_z orbital (see in Fig.2.7(b)). In the calculations, atomic defects are modelled as randomly distributed vacancies, where the p_z orbitals are simply removed from the honeycomb lattice not to allow the hopping to the vacancy sites. This actually mimics the hybridization of the corresponding p_z orbital with a hydrogen adatom if the corresponding Gaussian potential function would be taken with a very narrow width and very high amplitude. In our calculations, lattice distortion effects due to hydrogenation are neglected and zigzag edge atoms are taken to be free of defects, assuming a controlled hydrogenation of nanoribbon's bulk region only.

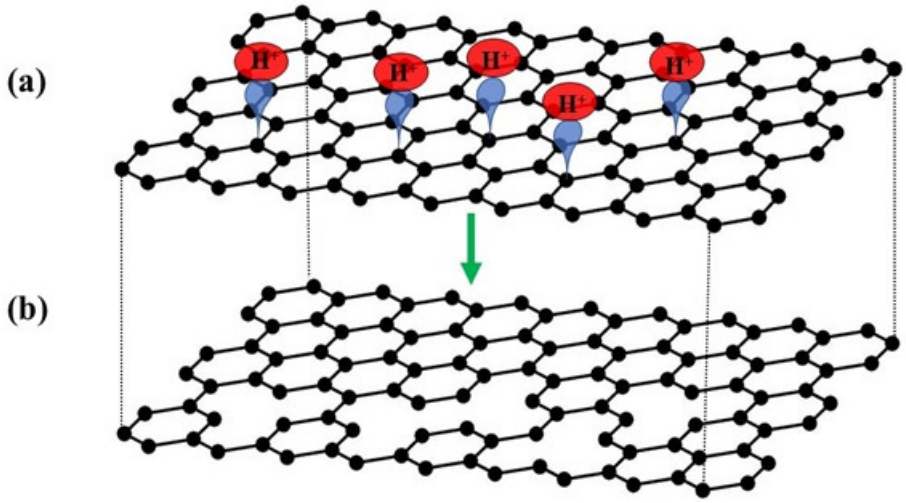

Figure 2.7. (a) Hydrogenation of a p_z orbital. (b) Projection of (a) in terms of vacancies

2.2.3. Anderson Localization

In the quantum statistical mechanics, if one creates a density fluctuation (wave packet) and leave it spread over the ribbon, it would be expected not to localize at any regions in the system. This behaviour is partially related to the classical random walk stated by the diffusion equation of Einstein in 1905 (Albert (1905)). This diffusion equation is valid only for random walk provided that there is no memory (also known as markovian process). In this equation with the demonstration of Einstein, localization of the wave packet should be proportional to the time with a prefactor of diffusion constant. However, before 60 years from now, P. W. Anderson (Anderson (1958)) considered this equation with the quantum particles (states), and then stated that there may be some situations for the quantum particles that the localization of the wave packet will not keep increasing forever and tending to infinity, instead, it can tend to a constant, which would mean that the diffusion constant is exactly zero. Therefore, the two considerations for a system, which consists of randomly distributed disorders, can be considered as correct for different situations, if one look at Einstein's arguments is valid for random walk which has no memory and also if one is dealing with quantum particles then quantum random walk, which has memory in it, should probably be used by the Anderson arguments. The localized wavefunction can be written in terms of the basis states of the system which are defined as

Bloch wavefunctions before,

$$\Psi = e^{-\frac{r}{\lambda}} \sum_i C_i \psi_i(\mathbf{r} - \mathbf{r}_i) \tag{2.50}$$

where λ is the localization length and the summation is over all sites. If the system does not include any disorders, then the λ would go to infinity and this wavefunction becomes a Bloch wavefunction. On the other hand, if we have a finite λ, then it means that we have a localized wavefunction defined as above.

In principle, there are infinitely models of disorder, which we have given in just two classifications before, randomly located impurities, lattice models, etc. However, the original model that Anderson proposed is with random potential model. In this model, we have on-site randomly distributed disorders which means that each sites of the lattice can cause an eigenstate for a particle, only difference from the TB model which we discussed is that the randomly chosen sites energies are not equal to each other due to the on-site disorder. What Anderson proposed in the work (Anderson (1958)), a considering situation, is that on-site potential is randomly picked and defined between a minimum and a maximum parameters as a disorder strength in terms of hopping parameter, then there is a critical value for the on-site matrix elements in the TB Hamiltonian, and due to the essential randomness the on-site energies vary from site to site. These energies would be a value which is smaller than the critical value, then Anderson insulator takes place. On the contrary, if this value would be higher than the critical value, then what we are dealing with is a metal. This is a consequence of the existence of localization states by Anderson's argument. This result can also be obtained by considering the conductivity in the system. If there is a localized state in the system, then the wavefunctions, which are localized, cannot contribute to the global transport, and eventually conductivity of the system would decrease or vanishes (Thouless (1970)). After the stimulating discussions and correspondence to the Anderson's argument by the studies of Ziman, Nevill Mott and Lloyd (Ziman (1969),Mott (1967),Lloyd (1969)), Thouless simplified the Anderson's argument to the statistical mechanics. After a few years, Anderson et. al. showed metal-insulator transition with vanishing conductivity (Abrahams et al. (1979)).

In this part of the work, we show that concentration of vacancies may induce a metal to insulator transition in finite ZGNRs by using mean-field Hubbard approximation. Indeed, it is mostly believed that short-range (Aleiner and B Efetov (2007), Altland (2006)) and strong long-range (Zhang et al. (2009)) disorder can give rise to intervalley scattering and Anderson localization, whereas weak long-range disorder can only lead

to intravalley scattering, that does not cause backscattering and Anderson localization (Fan et al. (2014)). Because of the vacancies break the sublattice symmetry, and intervalley scattering backscattering should be observed and if the concentration number is high enough, localized wavefunction should be observed (Güçlü et al. (2014),Ostrovsky et al. (2007),Bardarson et al. (2007)) with zero conductivity.

CHAPTER 3

RESULTS AND DISCUSSION

In order to find the overall ground state energy for each magnetic configuration, we need to employ a self-consistent pattern as, for a given S_z or σ , the energy depends on the density matrices $\langle n_{ij\sigma} \rangle$, which may be also known as the mean occupation number of that S_z configuration. In our calculations both for TB and MFH hopping parameters are taken as $t_{nn} = -2.8eV$ for the nearest neighbors and $t_{nnn} = -0.1eV$ for the second nearest neighbors (Castro Neto et al. (2009),Reich et al. (2002)). The self-consistent Hubbard calculations were performed within different $S_z = ((n_\uparrow - n_\downarrow)/2$ subspaces to find the overall ground state. As one may suspect a competition between the AFM and FM states, we have scanned the $0 \leq S_z \leq 130$ values, with a focus around AFM state $S_z = 0$ and FM state $S_z = N_{edge}/2$ where the number of edge states is given by $N_{edge} = 138$ for the clean structure. For each value S_z the self consistent calculations were repeated with different initial density matrices to ensure the convergence to the global energy minimum.

3.1. Computational Details

If we transform the calculation from the Eq.(2.48) into the matrices for only up-electrons,

$$H^{\uparrow}_{MFH} = \begin{bmatrix} H^{\uparrow}_{int} & t_{nn} & 0 & 0 & t_{nnn} & \dots & t_{nn} \\ t_{nn} & H^{\uparrow}_{int} & t_{nn} & 0 & 0 & \ddots & \vdots \\ 0 & t_{nn} & H^{\uparrow}_{int} & t_{nn} & 0 & \cdots & t_{nnn} \\ 0 & 0 & t_{nn} & H^{\uparrow}_{int} & t_{nn} & \cdots & 0 \\ t_{nnn} & 0 & 0 & t_{nn} & H^{\uparrow}_{int} & \ddots & \vdots \\ \vdots & \ddots & \vdots & \vdots & \ddots & \ddots & t_{nn} \\ t_{nn} & \cdots & t_{nnn} & 0 & \cdots & t_{nn} & H^{\uparrow}_{int} \end{bmatrix}_{N \times N} \tag{3.1}$$

The on-site Coulomb potential U is taken to be $16.522/\kappa eV$ where $\kappa = 6$ an effective dielectric constant, as was shown before in Eq.(2.27). The long-range interaction parameter V_{ij} are taken to be $8.64/\kappa eV$ and $5.33/\kappa eV$ for the first two neighbors, and $1/d_{ij}\kappa$

for distant neighbors (Potasz et al. (2010)) in Eq.(2.33). The effect of long-rage Coulomb interactions is found to be negligible in the presence of atomic defects considered in this work.

$$V_{ij} = \begin{bmatrix} 0 & V_{nn}^{rep} & D & D & V_{nnn}^{rep} & \dots & D \\ V_{nn}^{rep} & 0 & V_{nn}^{rep} & D & D & \ddots & \vdots \\ D & V_{nn}^{rep} & 0 & V_{nn}^{rep} & D & \cdots & V_{nnn}^{rep} \\ D & D & V_{nn}^{rep} & 0 & V_{nn}^{rep} & \cdots & D \\ V_{nnn}^{rep} & D & D & V_{nn}^{rep} & 0 & \ddots & \vdots \\ \vdots & \ddots & \vdots & \vdots & \ddots & \ddots & V_{nn}^{rep} \\ V_{nn}^{rep} & \cdots & V_{nnn}^{rep} & D & \cdots & V_{nn}^{rep} & 0 \end{bmatrix}_{N\times N} \tag{3.2}$$

$D = 1/\kappa d_{ij}$,off-site Coulomb repulsion between distant neighbors

$V_{nn}^{rep} = 8.64/\kappa$,off-site Coulomb repulsion for nearest neighbors

$V_{nnn}^{rep} = 5.33/\kappa$,off-site Coulomb repulsion for next nearest neighbors

$$V_{int} = \Big[V_{ij}\Big]_{N\times N}\Big[(\langle n_i\rangle - 1)\Big]_{N\times 1} = \begin{bmatrix} V_{int}^{1} \\ \vdots \\ V_{int}^{N} \end{bmatrix}_{N\times 1}$$

And finally,

$$H_{int}^{\uparrow} = \Big\{U\Big(\langle n_{i\uparrow}\rangle - \frac{1}{2}\Big) + V_{int}^{i}\Big\}_{N\times 1} = \begin{bmatrix} H_{int}^{\uparrow}(1) \\ \vdots \\ H_{int}^{\uparrow}(N) \end{bmatrix}_{N\times 1} \tag{3.3}$$

Hence, some initial parameters (in Eq.(3.3)) of the self-consistent calculations are fixed initially and never changes, later. However, some other initials such as,$N_{\uparrow}$, $N_{\downarrow}$, step parameter, and some techniques that we used to speed up the computational processes are not fixed for a magnetic configuration. We called the methods as "the shifting techniques" which are some extra initial perturbations that we applied in agreement with our expectation such as pulling or pushing all the electrons to the edges. These methods are included just to make the process faster and we found that only FM-states need this method. Therefore, we do not use any shifting techniques for AFM-state calculations for $S_z = 0$.

In more details, we proceeded as follows: it is simpler to numerically diagonalize the Hamiltonian of Eq.(3.1), in order to determine eigenvalues $\varepsilon_\sigma(i)$, and eigenvectors

$\left|\Psi^i_{p\sigma}\right\rangle = \sum_p A^i_{p\sigma} \left|\psi_{p\sigma}\right\rangle$ (with i = 1, 2 .... N_σ). Indeed, we worked with the chemical potential and Fermi-Dirac distribution functions, since it is common practice which is characterized by a temperature parameter T different from zero. The calculations are performed in the frames 3, 4, 5, and 6 are based on equations Eq.(3.4), Eq.(3.5), Eq.(3.6), and Eq.(3.7) given below. The first of these equations expresses the chemical potential and Fermi-Dirac distribution, $\mu_\sigma(i)$, and $f_\sigma(i)$, respectively.

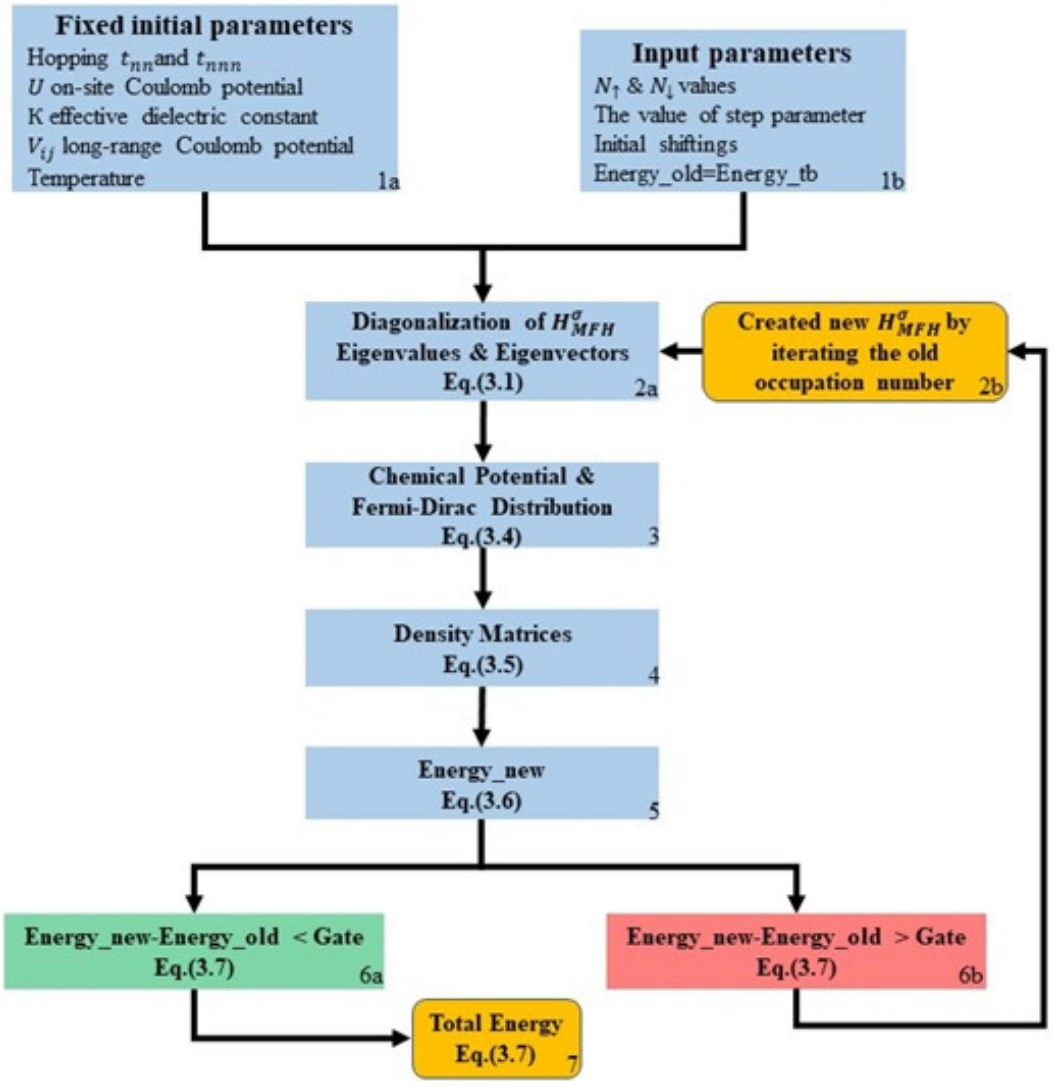

Figure 3.1. Pattern of the self-consistent algorithm leading to the ground state phase diagram of Figure 3.7. Equations are described in the text

Here, $\beta = 1/k_B T$ is Boltzmann factor and we have defined the by using Eq.(3.4) and Eq.(3.5) the density matrices for up-down electrons.

$$\mu_\sigma = \big(\varepsilon_\sigma(N_\sigma) - \varepsilon_\sigma(N_\sigma + 1)\big)/2 \tag{3.4}$$

$$f_\sigma(\varepsilon_i) = \frac{1}{1 + e^{\beta \times \left(\varepsilon_\sigma(i) - \mu_\sigma(i)\right)}} \tag{3.5}$$

Finally, the mean occupation number per site i and per spin σ at a given temperature T is given by:

$$\big\langle n_{i\sigma} \big\rangle = diag(\rho_\sigma(i,j)) = diag\bigg[\sum_{p=1}^{N_\sigma} \big\langle \Psi^i_{p\sigma} | f_\sigma(\varepsilon_i) | \Psi^i_{p\sigma} \big\rangle\bigg] \tag{3.6}$$

Eventually, the way to find the total energy E of a system in quantum mechanics, we should find the expectation value of each terms in the Hamiltonian of Eq.(3.1);

$$\begin{aligned}
E_{tb} &= \big\langle H_{tb} \big\rangle = Tr\big\{H'_{tb}\rho_\sigma(i,j)\big\} \\
E^{on-site}_{int} &= \big\langle H^{on-site}_{int} \big\rangle = U\bigg\{diag(\rho_\sigma(i,j) - \frac{1}{2})' diag(\rho_\sigma(i,j) - \frac{1}{2})\bigg\} \\
E^{off-site}_{int} &= \big\langle H^{off-site}_{int} \big\rangle = \frac{1}{2}\bigg\{diag(\rho_\sigma(i,j) - 1)' V_{ij} diag(\rho_\sigma(i,j) - 1)\bigg\} \\
E_{ground-state} &= E_{tb} + E^{on-site}_{int} + E^{off-site}_{int}
\end{aligned} \tag{3.7}$$

In general, we computed the ground-state energy for each magnetic state by playing with the initial parameter which are not fixed. The magnetic phases appear according to their S_z values. However, if $S_z = 0$ in the clean ZGNR, there can be seen full antiferromagnetic coupled edges, but if $S_z = 69$, then there must be seen full ferromagnetic coupled edges for the system. Therefore, now we can discuss the disordered systems.

3.2. Short-Range Disorder Analyse

We consider 55.83 nm long and 4.54 nm wide ZGNRs consisting of 10010 atoms with various defect configurations. ZGNR with this length has 138 edge states for the clean case. Fig.(3.2a) shows a ZGNR configuration with 1% of defects that are randomly distributed among the two sublattice of the honeycomb lattice. The downward pointing (blue color) and upward pointing (red color) triangles correspond to sublattice A-site and B-site vacancies, respectively. The left 10.5 nm part of the ribbon is left for the Anderson

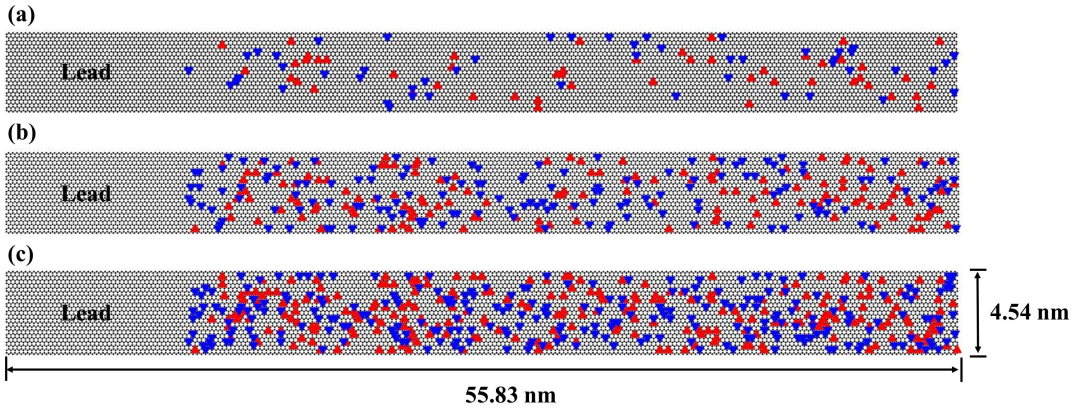

Figure 3.2. Structure and (a)1% (b)3% (c)5% defect distribution equally distributed with A-sublattice (downward pointed triangles) and B-sublattice (upward pointed triangles).

localization calculations. Initial electron waves started to diffuse through the ribbon from the lead part, where there is no impurity effect is considered.

3.2.1. Electronic Properties

Within in the tight-binding approximation, there is no information about spin dependency of the states. However, we can see the net charge localized points for the edge and defects states. Fig.(3.3) shows the electronic densities of the highest 69 (edge) states and highest 139 states densities all over the disordered ribbon by 1% vacancy concentration. Firstly, these TB and MFH results indicate while there is less defect states close to the Fermi level in the TB approach than the MFH results. However, if we include lowest valence states into the calculation, then we can get more density of defect states, that's why TB calculations have no spin information and due to the fact that even if we break the sublattice symmetry and the local magnetization could be induced in the vicinity of the defects, we cannot get higher densities by taking only the states near the Fermi level, we have to take into account deep valence states. On the other hand, while the edge states (Fig.(3.3-left panels)) are robust against the vacancies (Fig.(3.2a)) in the density of highest valence states, the impurity states begin to appear in the density of deep valence states. Whereas, tight-binding model gives quite good approximation to the real results,

the results always are lacking spin dependency. However, in the Fig. (3.3-right panels), while electron-electron interactions are included, the interaction effects carry the impurity states to the more energetic valence states, and we can get more density of impurity states in the upper panel, now.

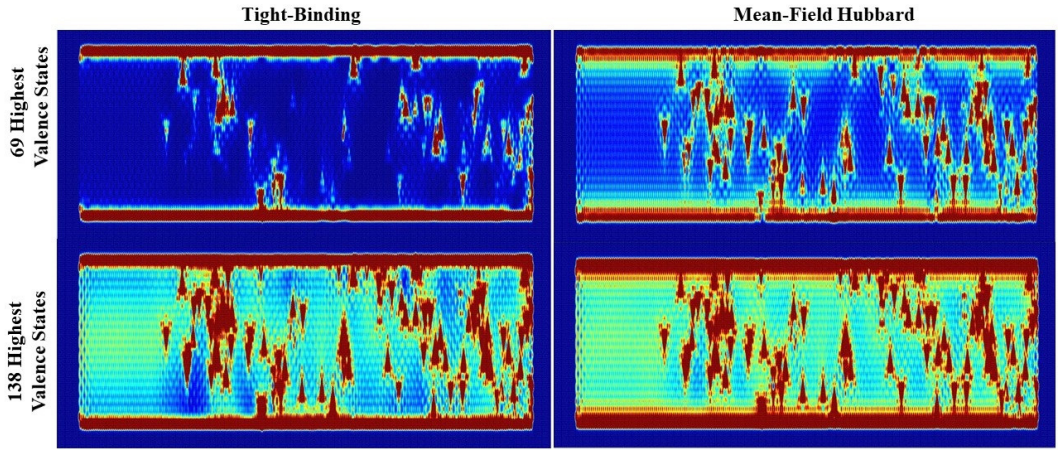

Figure 3.3. Electronic density profile corresponding to the 69 highest occupied valence states (top panels), and the 138 highest occupied valence states (bottom panels), obtained using tight-binding (left panels) and mean-field Hubbard calculations (right panels).

Therefore, whereas the electron-electron interactions make the defect states robust, which means defect-defect interactions begin to play at the same time, also the edge states becomes more fragile against the disorders. Because of this fact that MFH results give more realistic spin-dependent density characteristics for the system. Fig.(3.4) shows the near of the Fermi level in the clean and up to 5% disordered systems. As we discussed above, in the TB approach, there are edge states at the Fermi level and if we include the vacancies randomly, there will be impurity states close to the Fermi level. There is a big peak in the Fermi level and it's raising up to the 5% vacancy concentrations. These peaks around Fermi level are due to the impurity states (and initially edge states) in agreement with the earlier studies (Wakabayashi et al. (1998),Pereira et al. (2008), (KAN et al., 2008)). This single peaks splits into two within the MFH calculation when we include the interactions. We will discuss the magnetic properties of the system in the next subsection.

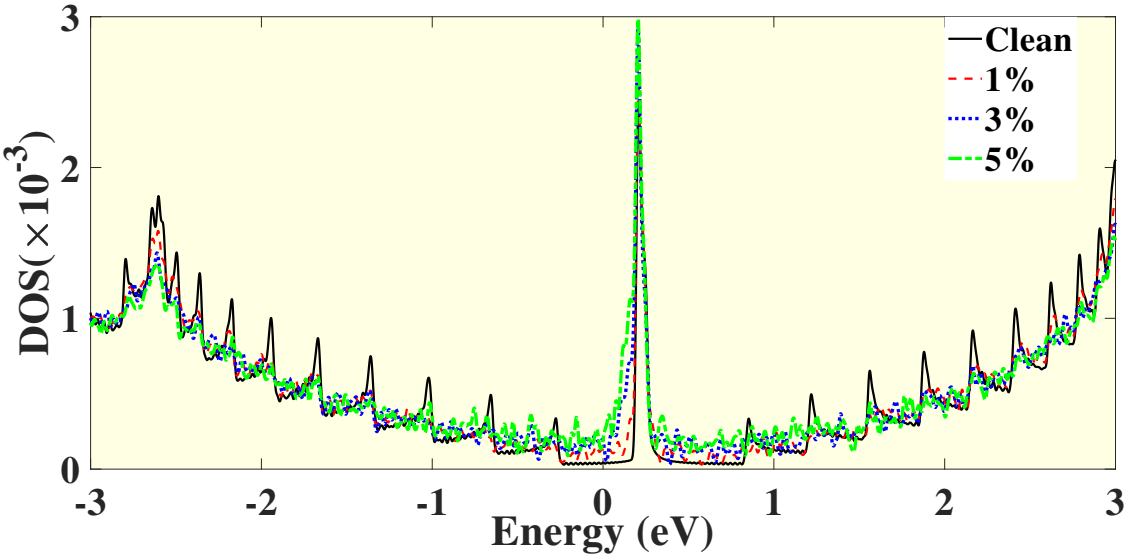

Figure 3.4. Dos of ZGNR by tight-binding results around the Fermi level.

3.2.2. Magnetic Properties

In this section, the combined effect of atomic disorders and electron-electron interactions to the system will be discussed. In Fig.(3.5), the electronic band structure is given for different vacancy concentration. As we discussed previous section, the edge states split into two separate peaks around the Fermi level, giving rise to edge states at the zigzag edges due to the electron-electron interactions. One can also state from the figure that the fluctuations of the electronic band diagram are getting suppressed due to the disorder effects for the system.

Fig.(3.6) shows the spin densities of the ribbon in Fig.(3.1a), for the lowest energy AFM and FM states, respectively. Despite the inclusion of long range electron interactions and second nearest neighbor hoppings, the mean-field solution to the Hubbard model leads to $S_z = 0$ ground state in all our calculations with equally distributed defects among the two sublattices, in agreement with Lieb's theorem (Lieb (1989)). Indeed, in Fig.(3.6a), the A-site and B-site defects lead to spin-up (red color) and spin-down (blue) magnetic moments, respectively, as expected. On the other hand, the spin density distribution for the lowest FM state is harder to predict since it is not a ground state consistent with Lieb's theorem. Interestingly, the edge ferromagnetism of the $S_z = 73$ state remains robust

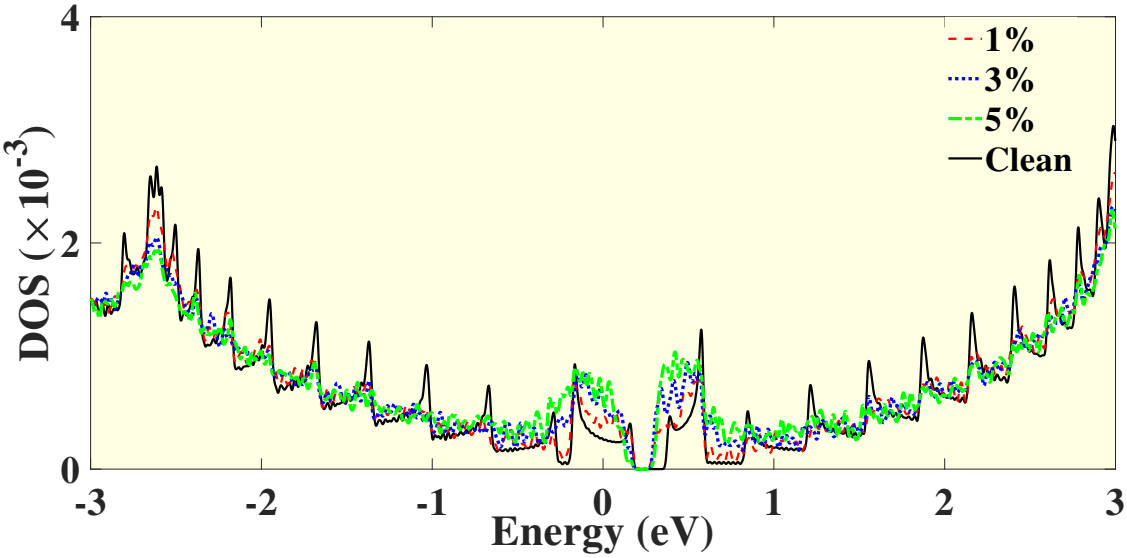

Figure 3.5. Dos of ZGNR by mean-field Hubbard results around the Fermi level.

(see Fig.(3.6b)) and the bulk atoms have a zero-average magnetization(Fig(3.7)). This simple observation has an important consequence on the stability of the AFM phase with respect to the FM phase: For the FM phase, the magnetization of the defects nearby edge atoms is strictly dictated by the strong magnetization of the edges, locally obeying Lieb's theorem. Hence far from the edges, one must encounter sublattice spin frustrations where Lieb's theorem cannot be locally satisfied, costing energy. For instance, for the AFM state where the Lieb's theorem is globally satisfied, the A-site defects in the encircled areas in Fig.(3.6a) are ferromagnetically coupled to each other, whereas their coupling is antiferromagnetic in Fig.(3.6b). Our calculations show that such local violation of Lieb's theorem only occurs among defect sites and never between an edge and a defect site.

As discussed above, local violation of Lieb's theorem in the bulk region of the FM phase costs energy. A striking consequence of the energy cost is an increased stability of the AFM phase with respect to the FM phase. Fig.(3.8) shows that the energy per atom of different magnetic states S_z with respect to the AFM ground state, for various defect concentrations up to 5%. For clean structure, the FM phase is at $S_z = N_{edge}/2 = 69$ and the FM-AFM gap is $3.041 \times 10^{-5} eV/atom$. As the defect concentration is increased, the FM-AFM gap increases, reaching $1.6 \times 10^{-4} eV/atom$ for the 5% of defects. Surprisingly, the gap increase with respect to the AFM phase occurs not only for FM phase but most other S_z states. However, in the vicinity of $S_z = 0$ (see the inset), i.e. for single/few spin

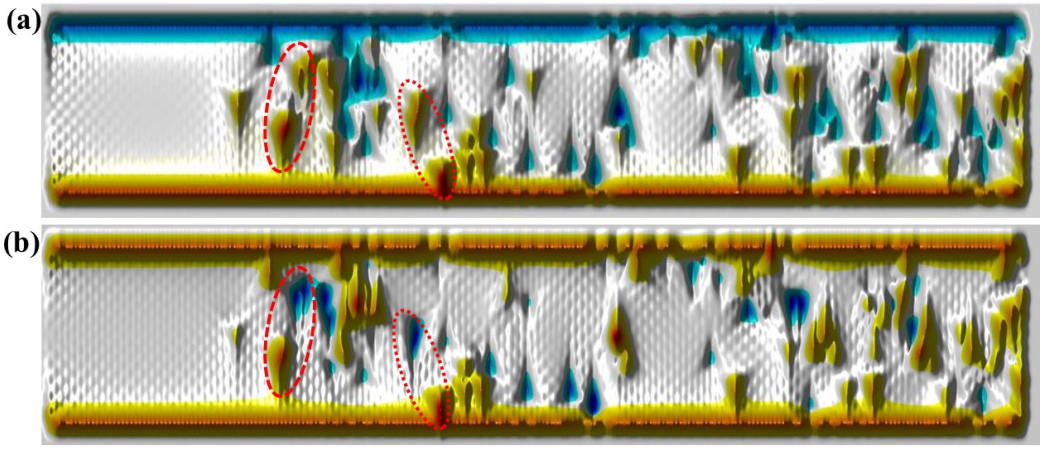

Figure 3.6. Magnetic density profile of (a) AFM and (b) FM state of the ribbon in Fig.(3.1a).

flips, energy cost is decreased at 1% of defect concentrations, but then increases slightly with increasing number of defects. This reflects the fact that for low defect concentrations it is easier to flip an edge spin by moving it into a defect state than into the opposite edge. We note that similar behaviours were observed for other randomly generated defect concentrations and each result is presented below in Fig.(3.10a).

Figure(3.9) shows the mean-field density of states (DOS) of AFM ground state, for different concentrations considered in Fig.(3.8). The solid lines represent the total DOS, whereas the dotted and dashed lines represent the contribution from edge and defect atoms (more precisely, atoms neighbouring the defects/vacancies) to the DOS, respectively. For the clean nanoribbon, the AFM gap is 0.2143 eV, which roughly corresponds to the energy required to flip a single spin. As the defect concentration is increased to 1%, there is an increase of midgap state density and the AFM gap is decreased to 0.1176 eV. This is consistent with the single spin flips in the vicinity of $S_z = 0$ discussed in Fig.(3.8). When the concentration of defects is increased to 3%,and then to 5%, the AFM gap now increases slightly. This change of behaviour reflects the fact that for higher number of defects the magnetic coupling between defects is enhanced in average, stabilizing the magnetic configuration and making the spin flips harder. However, we note that, the AFM-FM gap monotonically increases with increasing midgap states due to the local violation of Lieb's theorem, as discussed earlier.

Up to this point, the results presented were obtained for particular randomly generated defect configurations. For a statistical analysis of our results, we have repeated

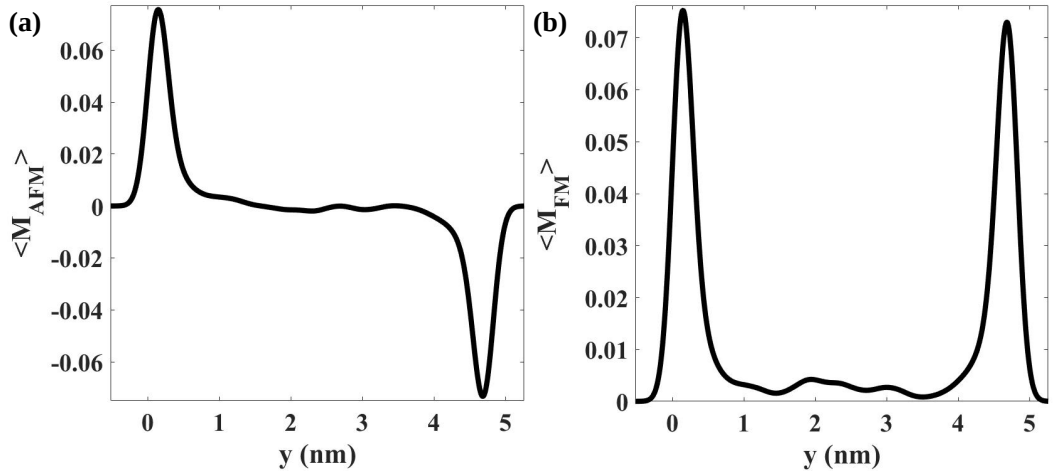

Figure 3.7. Average magnetization along the ribbon length for (a) the AFM in Fig.(3.6(a)) and (b) FM in Fig.(3.6(b)) phases.

our calculations for 10 randomly generated configuration at 1,3, and 5% defect concentrations. We have observed similar behaviour in all disorder configurations and the results are presented in Fig(3.10) as a function of defect concentration. The average magnetization of edge atoms for the AFM and FM phases, shown in Fig.(3.10(a)), decreases slightly with increasing defect concentration. The difference between the AFM and FM edge magnetization remains negligible (within the errors bars), consistent with Figs(**??**). On the other hand, Fig.(3.10(b)) shows that the AFM-FM gap rapidly decreases in average with a small error bar, clearly demenstrating an increased stability of the AFM phase with respect to the FM phase. Finally, the average AFM gap shown in Fig.(3.10(c)), indicating the energy cost for a single spin flip, systematically undergoes a decrease at lower concentrations, then keeps slowly increasing at concentrations higher than 1% due to a more stable magnetic lattice formed by defects.

3.2.3. Time Dependent MFH Solution

In this section we studied diffusion of the initial wavefunction through clean and disordered nanoribbons by solving the time dependent Schrödinger equation. Time dependent wavefunction equation can be written in terms of linear combination of MFH wavefunctions as,

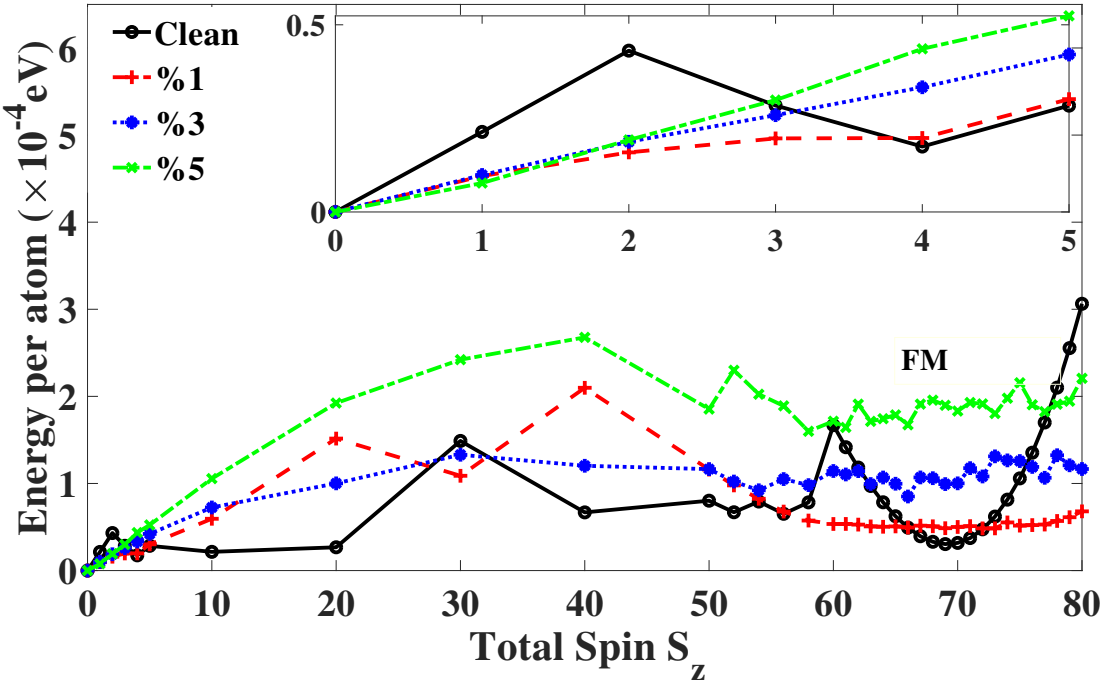

Figure 3.8. Mean-field energy per atom as a function of total spin S_z for clean, 1-3-5% of defect concentrations. For the clean case, the ground state is AFM phase with $S_z = 0$, and the FM phase occurs at $S_z = 69$. The FM-AFM gap increases with increasing defect.

$$|\Psi(t)\rangle = \sum_n C_n \, |\psi_n\rangle \, e^{-\frac{iE_n t}{\hbar}} \tag{3.8}$$

The coefficient C_n's can be evaluated only by taking $t = 0$ and by choosing any initial wavefunction $\Psi(t)$,

$$\langle \psi_n | \Psi(t) \rangle = C_n \langle \psi_n | \psi_n \rangle \tag{3.9}$$

We solved the time-dependent Scrödinger equation for different initial wavefunctions in each regions described in the Fig.(3.12), and we show the results in the following Figs.(3.14,3.15, 3.16,3.17,). In the first region in Fig.(3.12), away from the highest occupied valance states, inhomogeneous charge distribution and rarely defect state scattered sources are observed. An initial wave with energy -1.56 eV, which is in this region, is sent from the lead through all over the ribbon in Fig.(3.14). Since there are less defects in

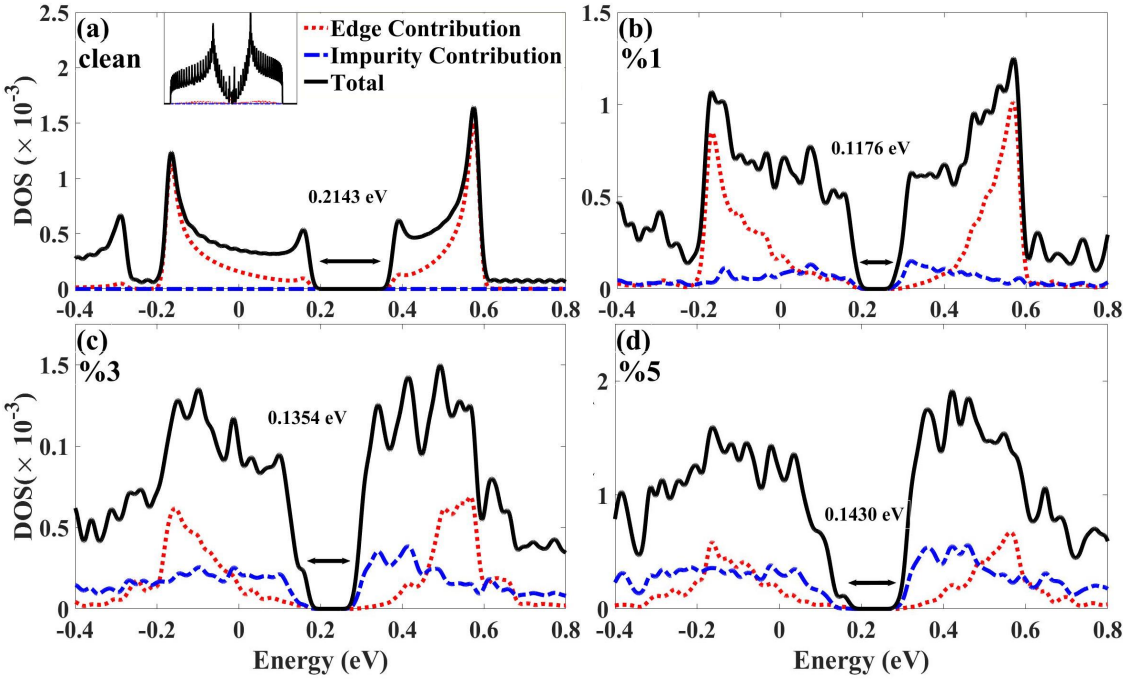

Figure 3.9. Mean-field DOS of the AFM phase for the (a) clean, (b) 1%, (c)3%, and 5% concentration cases. The contribution of edge and defect states are plotted with dotted and dot-dashed lines. Energy gap values of the total DOS are given for each case.

this region, the initial wave does not localized, and reaches to the end of the ribbon after a period of time. Therefore, there is no localization in this region.

In second region of Fig.(3.13), defect states are more visible. Electronic impurity density figure shows the electron-hole distribution around the vacancy regions. With an another initial wave with energy -0.77 eV in this region is diffused, and due to the fact that more defect(midgap) states can affect the initial wavefunction, the wave is getting hard to reach to the end of the ribbon.

In third region of Fig.(3.13), the population of edge states are more than defect states, initially. Impurity formation shows that there is no significant fragmentation at the edges. If we include more defect by increasing the vacancy concentration at the bulk region, then defect states will get more chance to be mixed with the edge states. However, since we don't allow the random vacancies to locate at the edges, we did not lose any edge states in the system. So, comparing with the clean system, more defects can affect more edge states at the edges due to the decreased distances between the defect and edge sites.

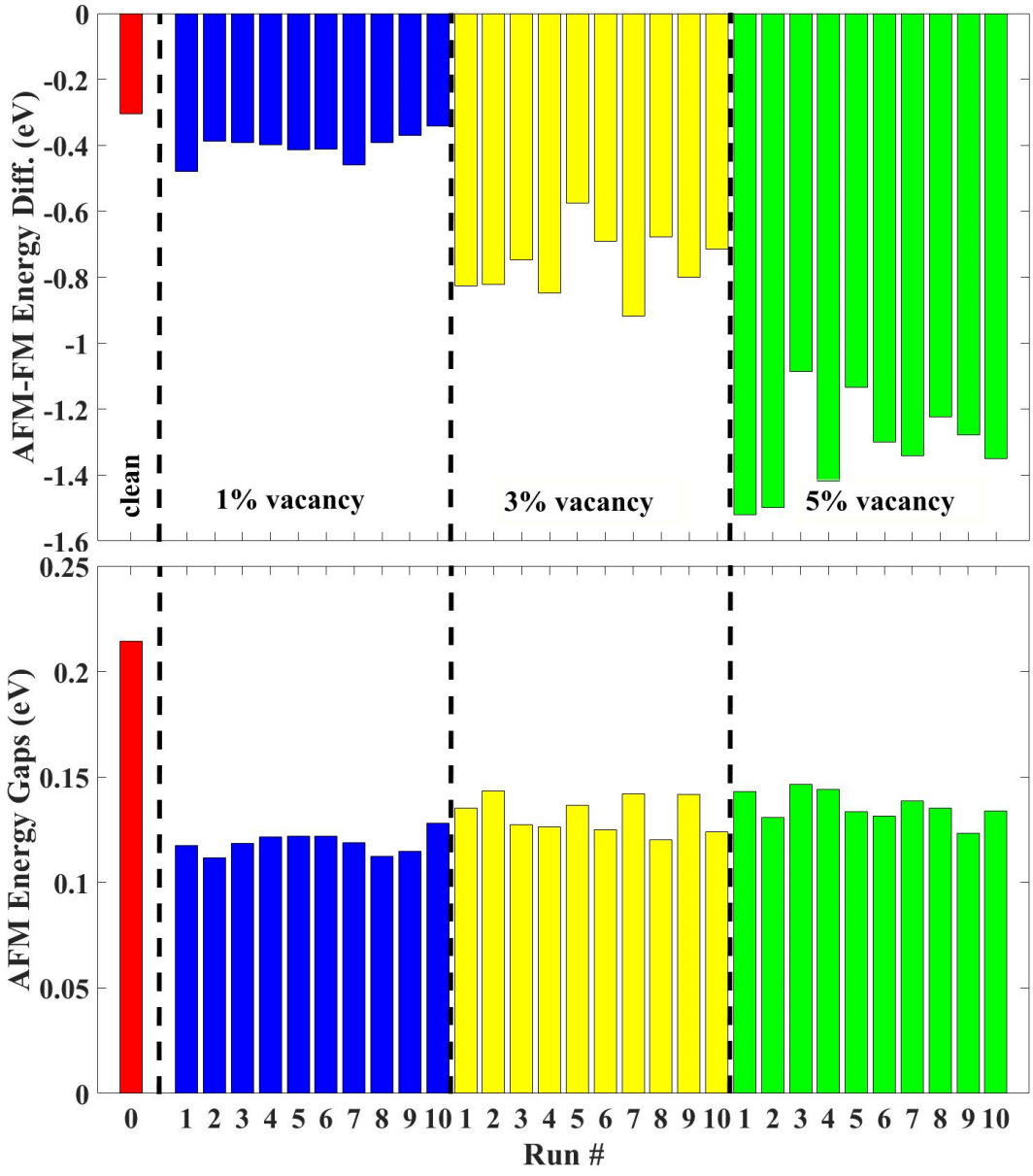

Figure 3.10. (a) Total Energy difference between the AFM and FM phases and (b) the antiferromagnetic phase energy gap for 30 different disorder configurations with various concentrations. Higher concentration effect causes the system to be more stable in antiferromagnetic state. For lower concentrations, the chance of a phase transition increases.

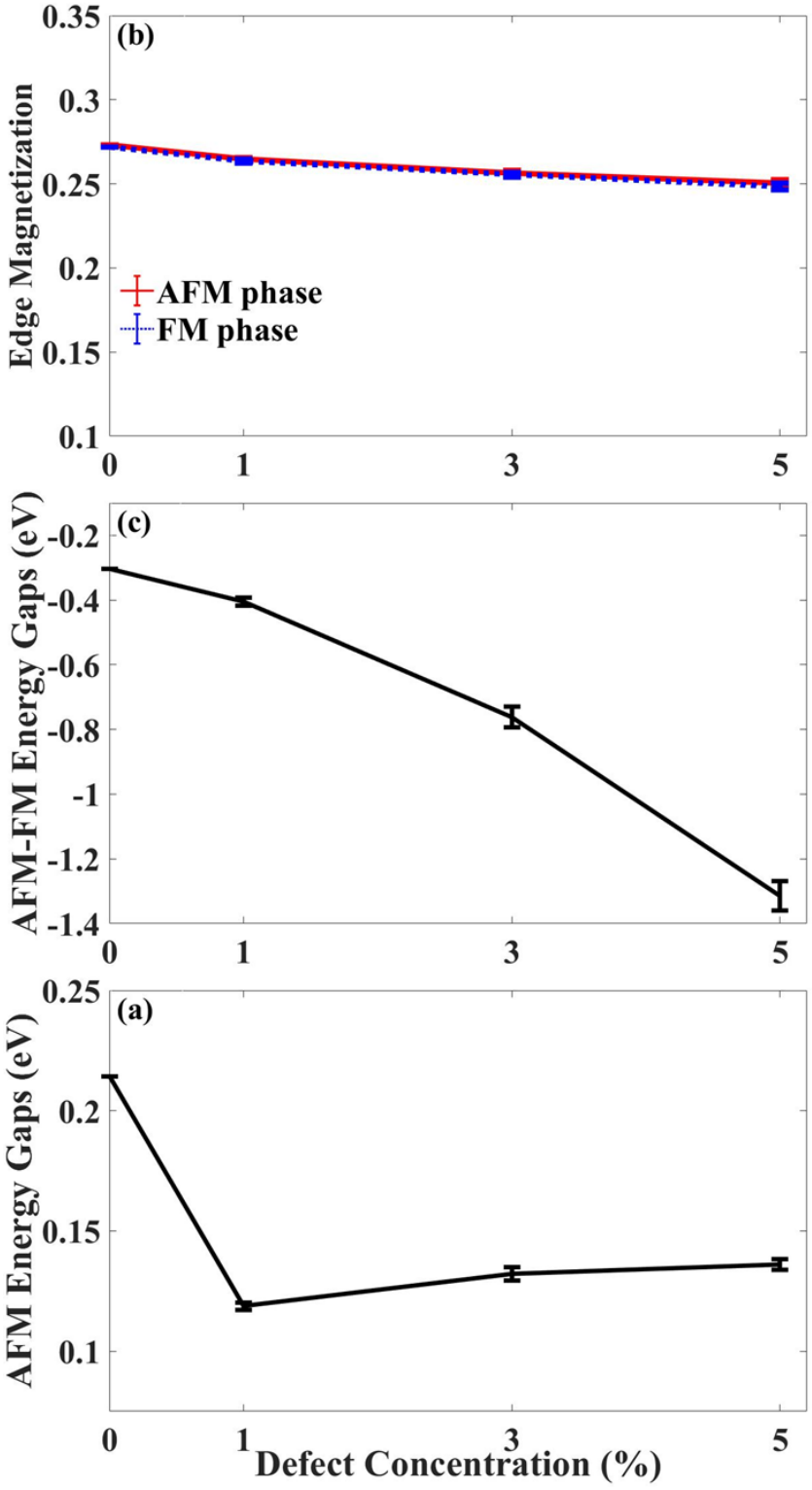

Figure 3.11. Average (a) single edge magnetization, (b) AFM-FM energy gap, and (c) AFM energy gap, over 10 randomly generated disorder configurations, as a function of defect concentration.

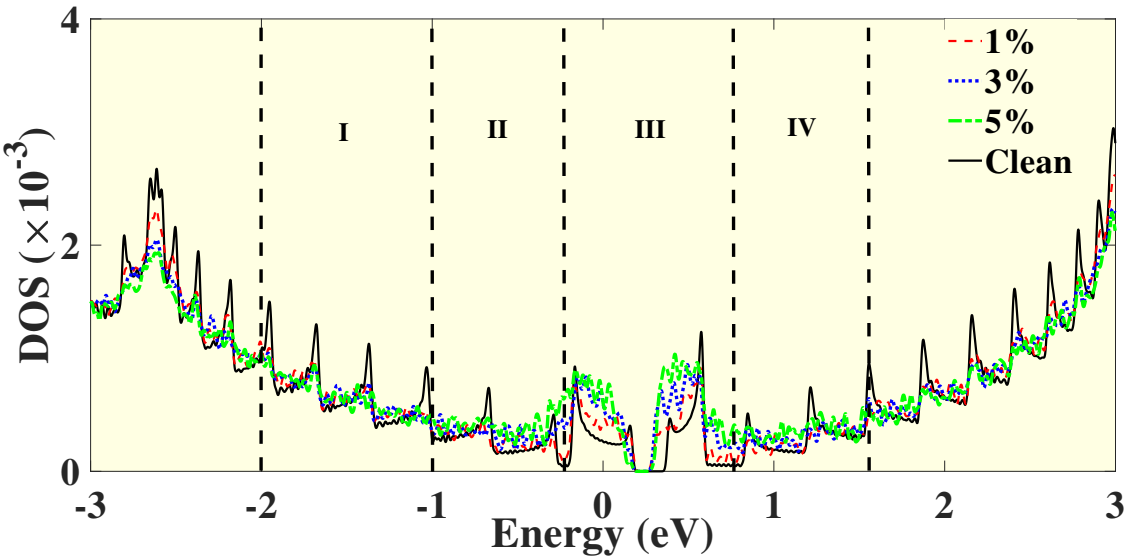

Figure 3.12. Red area, green, blue, black lines represents clean, 1-3-5% disordered DOS, respectively. Due to the randomness of the disorder's locations, 4 different regions are investigated.

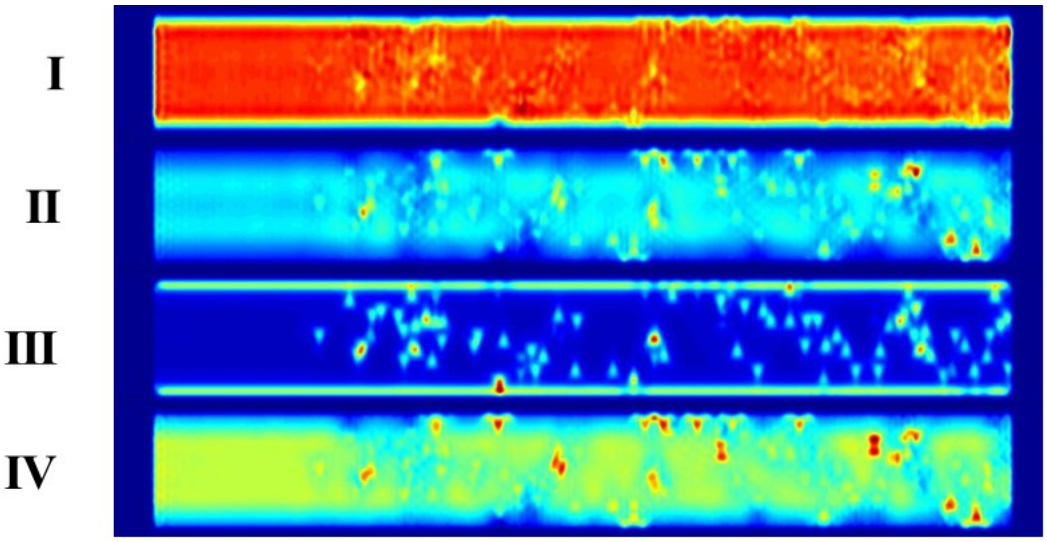

Figure 3.13. Impurity densities within four regions in Fig.(3.12)

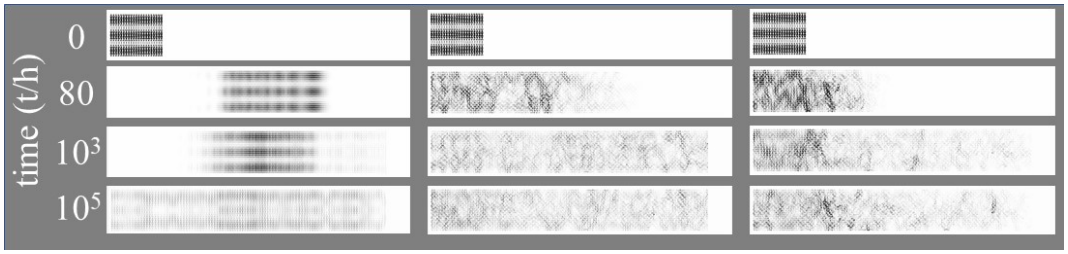

Figure 3.14. Clean (left), 1% (middle) and 3% (right) disordered time dependent solution of the wave function within region-I with incident particle energy -1.56 eV

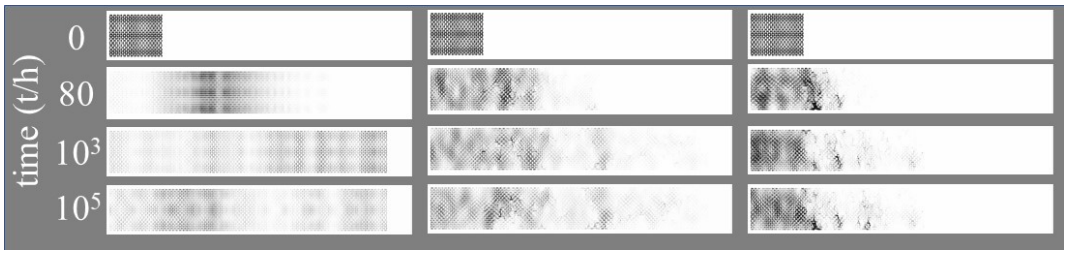

Figure 3.15. Clean (left), 1% (middle) and 3% (right) disordered time dependent solution of the wave function within region-II with incident particle energy -0.77 eV

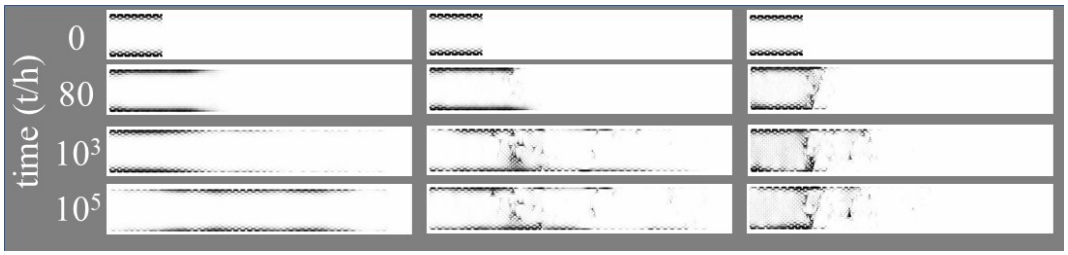

Figure 3.16. Clean (left), 1% (middle) and 3% (right) disordered time dependent solution of the wave function within region-III with incident particle energy -0.06 eV

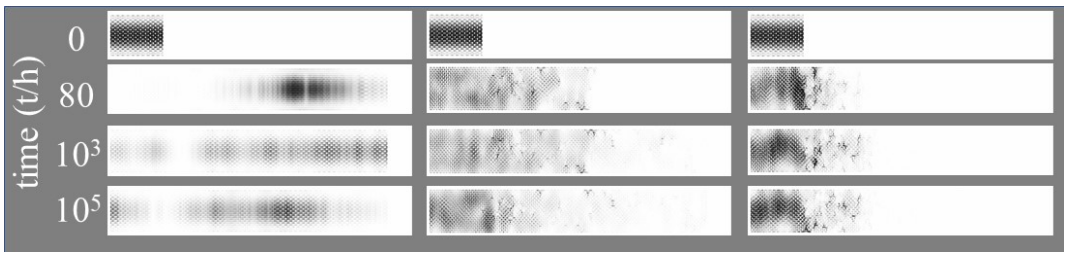

Figure 3.17. Clean (left), 1% (middle) and 3% (right) disordered time dependent solution of the wave function within region-IV with incident particle energy 1.10 eV

When an initial wave with energy -0.06 eV is diffused, in the middle of Fig.(3.16), the initial waves localized at the edges even after huge amount of time passed. We show that if the vacancy concentration is increased to 3%, then the localization length is decreased.

In fourth region of Fig.(3.13), the states belong to the lowest conduction bands. Due to the bulk region contribution is much higher than the edge states, we can see the impurity states more clear. Therefore, when an initial wave is sent from the lead with energy 1.10 eV, it has less chance to reach to the end of the ribbon than the other regions. Except the deepest valance states, localization in all regions with high concentration of vacancies exists.

To get more definite and quantitative result for localization length, the densities of quasistationary states by evaluating the initial wavefunctions in 10 steps around $t = 10^6/\hbar$ time point can be summed along the perpendicular direction to the diffusion direction. Fig.(3.18) shows the localization lengths with different vacancy concentrations in all four regions. It is obviously seen that, localization is much more weak in the deep valance states than the other regions. Other significant result is that, after 3% vacancy concentration, if we increased the number of vacancies region.III would have less localization length than region.II. This is because more vacancies can disrupt edge state densities and can block the transport over the region, as well. However, within the conduction band, defect-defect interaction is more strong than the edges. This caused strong localization here, as well.

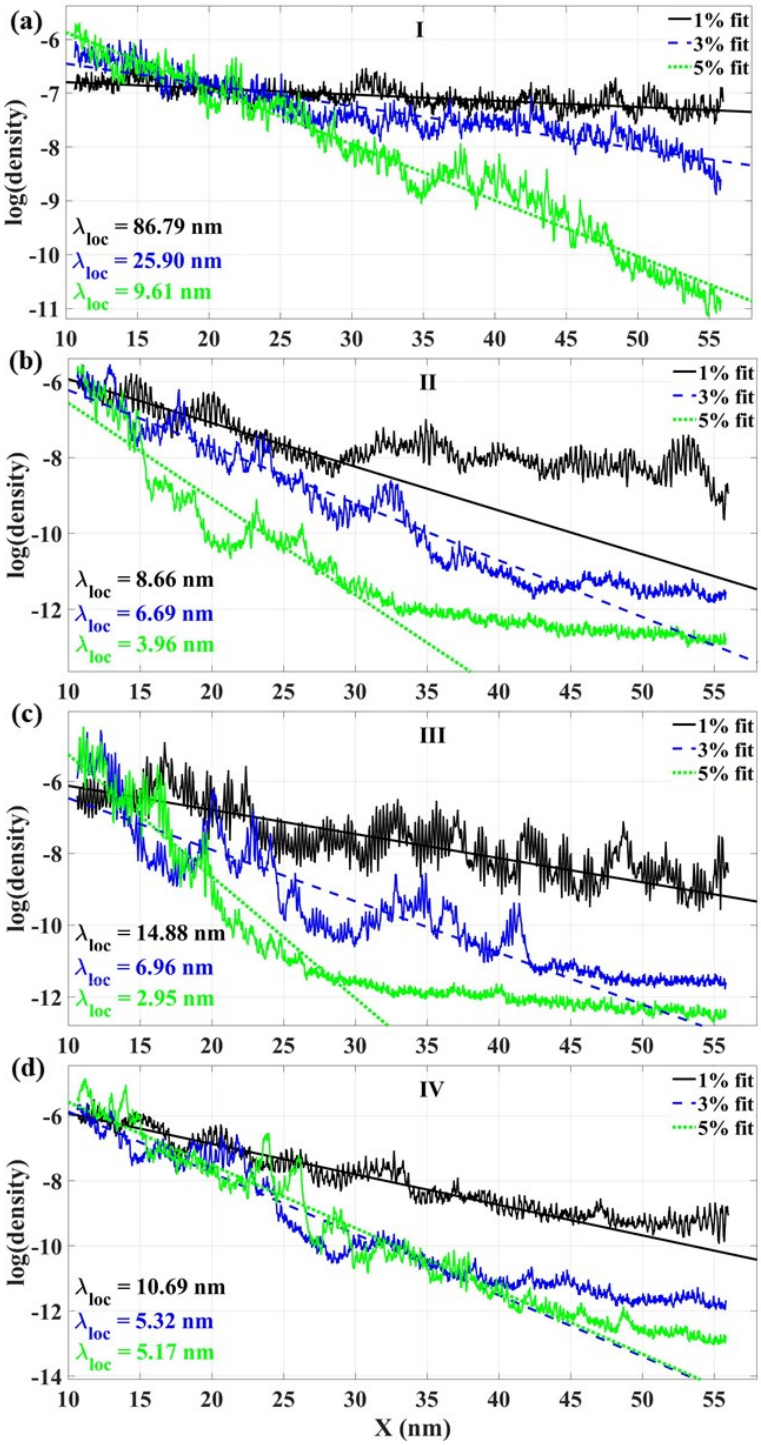

Figure 3.18. Localization lengths by time average solution with quasistationary states for (a) region-I (b) region-II (c) region-III (d) region-IV.

CHAPTER 4

CONCLUSION

In this thesis, we have studied the influence of random atomic disorders to the electronic structure and to the stability of magnetic structure of zigzag graphene nanoribbons by using mean-field Hubbard approximation and second nearest-neigbors are included. The electronic stability of edge states is found to be robust, since any vacancies is not located at the zigzag edges. However, if the vacancy concentration is increased, because of the distances between the defect sites and the edges decreased, the edge states can be weakened for higher concentrations. On the other hand, surprisingly, as the vacancy concentration is increased, the system get a more stable antiferromagnetic state with a total spin $S_z = 0$. Although the possibility of inducing magnetism due to the vacancies is well known from the previous works,for an equal distribution of atomic defects among the two sublattices of the honeycomb lattice, the ground state remains antiferromangetic with $S_z = 0$. Thus, the local magnetic moments can be induced, but globally our results show that the ground state is $S_z = 0$, in agreement with Lieb's theorem.At lower defect concentration ($\leq 1\%$), the energy of single spin flips from the antiferromagnetic ground state is decreased due to possible electron transfer from edges to defect states. However, we show that the AFM-FM energy gap remains well protected and is enhanced as a function defect concentration. The increased stability of the AFM-FM gap by controlling defect concentrations opens up new possibilities for spintronic and magnetic nanodevice applications.

Metal-insulator transition in agreement with Anderson's argument is investigated within mean-field Hubbard approach. We found that impurity states localized in the vicinity of the Fermi level, particularly $\big[-1.0, 1.0\big] eV$ interval. Localization length in this region is shorter than the other regions. For extreme limit of concentration(5%) of the vacancies only, we showed that the defect states and edge states are mixed and even if there is no vacancy at the edge sites, the transport along the edges is not possible. In other words, the system trying to preserve itself by converting the defect states to the edge states , however, this causes the conductivity goes to zero. However, the calculation of transport and conductance are left for the future works.

REFERENCES

Abrahams, E., P. W. Anderson, D. C. Licciardello, and T. V. Ramakrishnan (1979, Mar). Scaling theory of localization: Absence of quantum diffusion in two dimensions. *Phys. Rev. Lett. 42*, 673–676.

Albert, E. (1905). Uber die von der molekularkinetischen theorie der warme geforderte bewegung von in ruhenden flussigkeiten suspendierten teilchen. *Annalen der Physik 322*(8), 549–560.

Aleiner, I. and K. B Efetov (2007, 01). Effect of disorder on transport in graphene. *Physical review letters 97*, 236801.

Altland, A. (2006, Dec). Low-energy theory of disordered graphene. *Phys. Rev. Lett. 97*, 236802.

Anderson, P. W. (1958, Mar). Absence of diffusion in certain random lattices. *Phys. Rev. 109*, 1492–1505.

Awschalom, D. D., L. C. Bassett, A. S. Dzurak, E. L. Hu, and J. R. Petta (2013). Quantum spintronics: Engineering and manipulating atom-like spins in semiconductors. *Science 339*(6124), 1174–1179.

Bardarson, J. H., J. Tworzydło, P. W. Brouwer, and C. W. J. Beenakker (2007, Sep). One-parameter scaling at the dirac point in graphene. *Phys. Rev. Lett. 99*, 106801.

Berger, C., Z. Song, T. Li, X. Li, A. Y. Ogbazghi, R. Feng, Z. Dai, A. N. Marchenkov, E. H. Conrad, P. N. First, and W. A. de Heer (2004). Ultrathin epitaxial graphite 2d electron gas properties and a route toward graphene-based nanoelectronics. *The Journal of Physical Chemistry B 108*(52), 19912–19916.

Bostwick, A., J. L. McChesney, K. V. Emtsev, T. Seyller, K. Horn, S. D. Kevan, and E. Rotenberg (2009, Jul). Quasiparticle transformation during a metal-insulator transition in graphene. *Phys. Rev. Lett. 103*, 056404.

Cai, J., P. Ruffieux, R. Jaafar, M. Bieri, T. Braun, S. Blankenburg, M. Muoth, A. Seitsonen, M. Saleh, X. Feng, K. Müllen, and R. Fasel (2010, 07). Atomically precise bottom-up fabrication of graphene nanoribbons. *Nature 466*, 470–3.

Castro Neto, A. H., F. Guinea, N. M. R. Peres, K. S. Novoselov, and A. K. Geim (2009, Jan). The electronic properties of graphene. *Rev. Mod. Phys. 81*, 109–162.

Celebi, K., M. T. Cole, J. W. Choi, F. Wyczisk, P. Legagneux, N. Rupesinghe, J. Robertson, K. B. K. Teo, and H. G. Park (2013). Evolutionary kinetics of

graphene formation on copper. *Nano Letters 13*(3), 967–974. PMID: 23339597.

Cervantes-Sodi, F., G. Csányi, S. Piscanec, and A. C. Ferrari (2008, Apr). Edge-functionalized and substitutionally doped graphene nanoribbons: Electronic and spin properties. *Phys. Rev. B 77*, 165427.

Chao, K. A., J. Spalek, and A. M. Oles (1977). Kinetic exchange interaction in a narrow s-band. *Journal of Physics C: Solid State Physics 10*(10), L271.

Chappert, C., A. Fert, and F. Nguyen Van Dau (2007, 12). The emergence of spin electronics in data storage. *Nature materials 6*, 813–23.

Chen, Z., Y.-M. Lin, M. J. Rooks, and P. Avouris (2007). Graphene nanoribbon electronics. *Physica E: Low-dimensional Systems and Nanostructures 40*(2), 228 – 232.

Choi, W., I. Lahiri, R. Seelaboyina, and Y. S. Kang (2010). Synthesis of graphene and its applications: A review. *Critical Reviews in Solid State and Materials Sciences 35*(1), 52–71.

Crew, F. I. (02 March 2018). What is graphene? https://graphene-flagship.eu/material/graphene/Pages/What-is-graphene.aspx. Accessed:15 April 2018.

Dai Q.Q., Z. Y. F. and Q. Jiang (2013, Mar). Electronic and magnetic engineering in zigzag graphene nanoribbons having a topological line defect at different positions with or without strain. *The Journal of Physical Chemistry C 117*(9), 4791–4799.

Das Sarma, S., S. Adam, E. H. Hwang, and E. Rossi (2011, May). Electronic transport in two-dimensional graphene. *Rev. Mod. Phys. 83*, 407–470.

de Heer, W. A., C. Berger, X. Wu, P. N. First, E. H. Conrad, X. Li, T. Li, M. Sprinkle, J. Hass, M. L. Sadowski, M. Potemski, and G. Martinez (2007). Epitaxial graphene. *Solid State Communications 143*(1), 92 – 100. Exploring graphene.

Esquinazi, P., D. Spemann, R. Höhne, A. Setzer, K. Han, and T. Butz (2003, Nov). Induced magnetic ordering by proton irradiation in graphite. *Phys. Rev. Lett. 91*, 227201.

Exfoliation (2018). Exfoliation and lithography: Mechanical exfoliation.

Fan, Z., A. Uppstu, and A. Harju (2014, Jun). Anderson localization in two-dimensional graphene with short-range disorder: One-parameter scaling and finite-size effects. *Phys. Rev. B 89*, 245422.

Feldner, H., Z. Y. Meng, A. Honecker, D. Cabra, S. Wessel, and F. F. Assaad (2010, Mar). Magnetism of finite graphene samples: Mean-field theory compared with ex-

act diagonalization and quantum monte carlo simulations. *Phys. Rev. B 81*, 115416.

Fernández-Rossier, J. and J. J. Palacios (2007, Oct). Magnetism in graphene nanoislands. *Phys. Rev. Lett. 99*, 177204.

Fujita, M., K. Wakabayashi, K. Nakada, and K. Kusakabe (1996). Peculiar localized state at zigzag graphite edge. *Journal of the Physical Society of Japan 65*(7), 1920–1923.

Gargiulo, F., G. Autès, N. Virk, S. Barthel, M. Rösner, L. R. M. Toller, T. O. Wehling, and O. V. Yazyev (2014, Dec). Electronic transport in graphene with aggregated hydrogen adatoms. *Phys. Rev. Lett. 113*, 246601.

Geim, A. and K. Novoselov (2007, 3). The rise of graphene. *Nature Materials 6*(3), 183–191.

Gibertini, M., A. Tomadin, F. Guinea, M. I. Katsnelson, and M. Polini (2012, May). Electron-hole puddles in the absence of charged impurities. *Phys. Rev. B 85*, 201405.

González-Herrero, H., J. M. Gómez-Rodríguez, P. Mallet, M. Moaied, J. J. Palacios, C. Salgado, M. M. Ugeda, J.-Y. Veuillen, F. Yndurain, and I. Brihuega (2016). Atomic-scale control of graphene magnetism by using hydrogen atoms. *Science 352*(6284), 437–441.

Güçlü, A., P. Potasz, and M. Korkusinski (2014). *Graphene Quantum Dots*. Springer.

Güçlü, A. D. and N. Bulut (2015, Mar). Spin-spin correlations of magnetic adatoms on graphene. *Phys. Rev. B 91*, 125403.

Güçlü, A. D., P. Potasz, and P. Hawrylak (2013, Oct). Zero-energy states of graphene triangular quantum dots in a magnetic field. *Phys. Rev. B 88*, 155429.

Güçlü, A. D., P. Potasz, O. Voznyy, M. Korkusinski, and P. Hawrylak (2009, Dec). Magnetism and correlations in fractionally filled degenerate shells of graphene quantum dots. *Phys. Rev. Lett. 103*, 246805.

Han, M. Y., B. Özyilmaz, Y. Zhang, and P. Kim (2007, May). Energy band-gap engineering of graphene nanoribbons. *Phys. Rev. Lett. 98*, 206805.

Iijima, S. (1991, Nov). Helical microtubules of graphitic carbon. *Nature 354*, 56–58.

J., H. (1963). Electron correlations in narrow energy bands. *Proceedings of the Royal Society of London A: Mathematical, Physical and Engineering Sciences 276*(1365), 238–257.

Jaskólski, W., L. Chico, and A. Ayuela (2015, Apr). Divacancy-induced ferromagnetism in graphene nanoribbons. *Phys. Rev. B 91*, 165427.

Jean-Noel FUCHS, M. O. G. (2018, March). Introduction to the physical properties of graphene.

Jung, J. and A. H. MacDonald (2009, Jun). Carrier density and magnetism in graphene zigzag nanoribbons. *Phys. Rev. B 79*, 235433.

KAN, E., Z. LI, and J. YANG (2008). Magnetism in graphene systems. *Nano 03*(06), 433–442.

Kekule, F. A. (1865). Kekule's benzene structure. *Bulletin de la Societe Chimique de Paris 3*(2), 98.

Kimouche, A., M. M Ervasti, R. Drost, S. Halonen, A. Harju, P. M Joensuu, J. Sainio, and P. Liljeroth (2015, 12). Ultra-narrow metallic armchair graphene nanoribbons. *Nature communications 6*, 10177.

Klitzing, K. v., G. Dorda, and M. Pepper (1980, Aug). New method for high-accuracy determination of the fine-structure constant based on quantized hall resistance. *Phys. Rev. Lett. 45*, 494–497.

KROTO, H., J. HEATH, S. OBRIEN, R. CURL, and R. SMALLEY (1985, 11). C60: Buckminsterfullerene. *Nature 318*, 162–163.

L Wang, W., O. Yazyev, S. Meng, and E. Kaxiras (2009, 05). Topological frustration in graphene nanoflakes: Magnetic order and spin logic devices. *Physical review letters 102*, 157201.

Lee, H., Y.-W. Son, N. Park, S. Han, and J. Yu (2005, Nov). Magnetic ordering at the edges of graphitic fragments: Magnetic tail interactions between the edge-localized states. *Phys. Rev. B 72*, 174431.

Li, T. C. and S.-P. Lu (2008, Feb). Quantum conductance of graphene nanoribbons with edge defects. *Phys. Rev. B 77*, 085408.

Lieb, E. H. (1989, Mar). Two theorems on the hubbard model. *Phys. Rev. Lett. 62*, 1201–1204.

Lloyd, P. (1969, 05). Exactly solvable model of electronic states in a three-dimensional disordered hamiltonian: Non-existence of localized states. *Journal of Physics C: Solid State Physics 2*, 1717.

Magda, G. Z., X. Jin, I. Hagymasi, P. Vancso, Z. Osvath, P. Nemes-Incze, C. Hwang, L. P. Biro, and L. Tapaszto (2014, Oct). Room-temperature magnetic order on

zigzag edges of narrow graphene nanoribbons. *Nature 514*, 608–611.

Meany, L. J. and Joseph (2017). Graphene not just another miracle material. http://www.baen.com/graphene. Accessed: 2018-03-15.

Modarresi, M. and A. D. Güçlü (2017, Jun). Effects of interedge scattering on the wigner crystallization in graphene nanoribbons. *Phys. Rev. B 95*, 235103.

Mott, N. (1967). Electrons in disordered structures. *Advances in Physics 16*(61), 49–144.

NanoLab (2017).

Novoselov, K. S., A. K. Geim, S. V. Morozov, D. Jiang, M. I. Katsnelson, I. V. Grigorieva, S. V. Dubonos, and A. A. Firsov (2005, Nov). Two-dimensional gas of massless dirac fermions in graphene. *Nature 438*, 197–200.

Novoselov, K. S., A. K. Geim, S. V. Morozov, D. Jiang, Y. Zhang, S. V. Dubonos, I. V. Grigorieva, and A. A. Firsov (2004). Electric field effect in atomically thin carbon films. *Science 306*(5696), 666–669.

Ostrovsky, P. M., I. V. Gornyi, and A. D. Mirlin (2007, Jun). Quantum criticality and minimal conductivity in graphene with long-range disorder. *Phys. Rev. Lett. 98*, 256801.

Palacios, J. J., J. Fernández-Rossier, and L. Brey (2008, May). Vacancy-induced magnetism in graphene and graphene ribbons. *Phys. Rev. B 77*, 195428.

Pauling, L. (1960). *The Nature of Chemical Bonds*. Cornell UP.

Pereira, V. M., J. M. B. Lopes dos Santos, and A. H. Castro Neto (2008, Mar). Modeling disorder in graphene. *Phys. Rev. B 77*, 115109.

Potasz, P., A. D. Güçlü, and P. Hawrylak (2010, Aug). Spin and electronic correlations in gated graphene quantum rings. *Phys. Rev. B 82*, 075425.

Potasz, P., A. D. Güçlü, A. Wójs, and P. Hawrylak (2012, Feb). Electronic properties of gated triangular graphene quantum dots: Magnetism, correlations, and geometrical effects. *Phys. Rev. B 85*, 075431.

Reich, S., J. Maultzsch, C. Thomsen, and P. Ordejón (2002, Jul). Tight-binding description of graphene. *Phys. Rev. B 66*, 035412.

Ruffieux, P., S. Wang, B. Yang, C. Sánchez-Sánchez, J. Liu, T. Dienel, L. Talirz, P. Shinde, C. A. Pignedoli, D. Passerone, T. Dumslaff, X. Feng, K. Müllen, and R. Fasel (2016, Mar). On-surface synthesis of graphene nanoribbons with zigzag

edge topology. *Nature 531*, 489–492.

Schubert, G. and H. Fehske (2008, Jun). Dynamical aspects of two-dimensional quantum percolation. *Phys. Rev. B 77*, 245130.

Schubert, G. and H. Fehske (2012, Feb). Metal-to-insulator transition and electron-hole puddle formation in disordered graphene nanoribbons. *Phys. Rev. Lett. 108*, 066402.

Singh, R. and P. Kroll (2009, 05). Magnetism in graphene due to single-atom defects: Dependence on the concentration and packing geometry of defects. *Journal of physics. Condensed matter : an Institute of Physics journal 21*, 196002.

Son, Y.-W., M. L. Cohen, and S. G. Louie (2006, Nov). Energy gaps in graphene nanoribbons. *Phys. Rev. Lett. 97*, 216803.

Son, Y.-W., C. M. L., and L. S. G. (2006, Nov). Half-metallic graphene nanoribbons. *Nature 444*, 347 EP –.

Soriano, D., F. Munoz-Rojas, J. Fernandez-Rossier, and J. Palacios (2010, 01). Hydrogenated graphene nanoribbons for spintronics. *Physical Review B 81*, –.

Talirz, L., P. Ruffieux, and R. Fasel (2016, 02). On-surface synthesis of atomically precise graphene nanoribbons. *Advanced materials (Deerfield Beach, Fla.) 28*, –.

Tao, C., L. Jiao, O. Yazyev, Y.-C. Chen, J. Feng, X. Zhang, R. Capaz, J. Tour, A. Zettl, S. G. Louie, H. Dai, and M. F. Crommie (2011, 05). Spatially resolving edge states of chiral graphene nanoribbons. *Nature Physics 7*, 616–620.

Thouless, D. J. (1970). Anderson's theory of localized states. *Journal of Physics C: Solid State Physics 3*(7), 1559.

Topsakal, M., E. Aktürk, H. Sevinçli, and S. Ciraci (2008, Dec). First-principles approach to monitoring the band gap and magnetic state of a graphene nanoribbon via its vacancies. *Phys. Rev. B 78*, 235435.

U. Özdemir, H., A. Altintas, and A. D. Güçlü (2016, 01). Magnetic phases of graphene nanoribbons under potential fluctuations. *Physical Review B 93*, –.

Vancsó, P., I. Hagymási, and L. Tapasztó (2017). A magnetic phase-transition graphene transistor with tunable spin polarization. *2D Materials 4*(2), 024008.

Varchon, F., R. Feng, J. Hass, X. Li, B. N. Nguyen, C. Naud, P. Mallet, J.-Y. Veuillen, C. Berger, E. H. Conrad, and L. Magaud (2007, Sep). Electronic structure of epitaxial graphene layers on sic: Effect of the substrate. *Phys. Rev. Lett. 99*, 126805.

Wakabayashi, K., M. Sigrist, and M. Fujita (1998). Spin wave mode of edge-localized magnetic states in nanographite zigzag ribbons. *Journal of the Physical Society of Japan 67*(6), 2089–2093.

Wallace, P. R. (1947, May). The band theory of graphite. *Phys. Rev. 71*, 622–634.

Wang, X., Y. Ouyang, X. Li, H. Wang, J. Guo, and H. Dai (2008, May). Room-temperature all-semiconducting sub-10-nm graphene nanoribbon field-effect transistors. *Phys. Rev. Lett. 100*, 206803.

Wolf, S. A., D. D. Awschalom, R. A. Buhrman, J. M. Daughton, S. von Molnár, M. L. Roukes, A. Y. Chtchelkanova, and D. M. Treger (2001). Spintronics: A spin-based electronics vision for the future. *Science 294*(5546), 1488–1495.

Yazyev, O. V. (2008, Jul). Magnetism in disordered graphene and irradiated graphite. *Phys. Rev. Lett. 101*, 037203.

Yazyev, O. V. (2010). Emergence of magnetism in graphene materials and nanostructures. *Reports on Progress in Physics 73*(5), 056501.

Yazyev, O. V. and L. Helm (2007, Mar). Defect-induced magnetism in graphene. *Phys. Rev. B 75*, 125408.

Yazyev, O. V. and M. I. Katsnelson (2008, Jan). Magnetic correlations at graphene edges: Basis for novel spintronics devices. *Phys. Rev. Lett. 100*, 047209.

Yuanbo Zhang, Yan-Wen Tan, H. L. S. and P. Kim (2005, Nov). Experimental observation of the quantum hall effect and berry's phase in graphene. *Nature 438*, 201 EP –.

Zhang, Y., S.-Y. Li, H. Huang, W.-T. Li, J.-B. Qiao, W.-X. Wang, L.-J. Yin, K.-K. Bai, W. Duan, and L. He (2016, Oct). Scanning tunneling microscopy of the π magnetism of a single carbon vacancy in graphene. *Phys. Rev. Lett. 117*, 166801.

Zhang, Y.-Y., J. Hu, B. A. Bernevig, X. R. Wang, X. C. Xie, and W. M. Liu (2009, Mar). Localization and the kosterlitz-thouless transition in disordered graphene. *Phys. Rev. Lett. 102*, 106401.

Ziman, J. M. (1969). Localization of electrons in ordered and disordered systems ii. bound bands. *Journal of Physics C: Solid State Physics 2*(7), 1230.

APPENDIX A

PUBLICATIONS

- K. E. Çakmak, A. Altıntaş, A. D. Güçlü, Effects of random atomic disorder on the magnetic stability of graphene nanoribbons with zigzag edges, pre-print (arXiv: 1804.04645) (2018).
- A. Altıntaş, K. E. Çakmak, A. D. Güçlü, Effects of long-range disorder and electronic interactions on the optical properties of graphene quantum dots, Phys. Rev. B **95**, 045431 (2017).
- K. E. Çakmak, A. Altıntaş, A. D. Güçlü, Effects of atomic disorders on magnetic and electronic properties of zigzag graphene nanoribbons, 24th.IFG, June 2017, Oral Presentation.
- A. Altıntaş, H.U.Özdemir,K. E. Çakmak, A. D. Güçlü, Observation of Metal- Insulator Transition on Graphene Nanoribbons, 5th. Condensed Matter Meeting (YMF), Izmir, April 2016, Poster Presentation.
- K. E. Çakmak, Barış AKBALI, Electronic and Optical Properties of Graphene Quantum Dots, 3rd. GEFIK, 2014, Poster Presentation.